The Astrophysical Journal, 753:106 (21pp), 2012 July 10 doi:10.1088/0004-637X/753/2/106

A DESCRIPTION OF QUASAR VARIABILITY MEASURED USING REPEATED SDSS AND POSS IMAGING

Chelsea L. MacLeod[1], Željko Ivezić[1], Branimir Sesar[2], Wim de Vries[3], Christopher S. Kochanek[4,5], Brandon C. Kelly[6], Andrew C. Becker[1], Robert H. Lupton[7], Patrick B. Hall[8], Gordon T. Richards[9], Scott F. Anderson[1], and Donald P. Schneider[10,11]
[1] Department of Astronomy, University of Washington, Box 351580, Seattle, WA 98195, USA
[2] Division of Physics, Mathematics and Astronomy, California Institute of Technology, Pasadena, CA 91125, USA
[3] Department of Physics, University of California, One Shields Ave, Davis, CA 95616, USA
[4] Department of Astronomy, The Ohio State University, 140 West 18th Avenue, Columbus, OH 43210, USA
[5] The Center for Cosmology and Astroparticle Physics, The Ohio State University, 191 West Woodruff Avenue, Columbus, OH 43210, USA
[6] Department of Physics, University of California, Santa Barbara, CA 93106, USA
[7] Department of Astrophysical Sciences, Princeton University, Princeton, New Jersey 08544, USA
[8] Department of Physics and Astronomy, York University, Toronto, ON M3J 1P3, Canada
[9] Department of Physics, Drexel University, 3141 Chestnut Street, Philadelphia, PA 19104, USA
[10] Department of Astronomy and Astrophysics, The Pennsylvania State University, 525 Davey Laboratory, University Park, PA 16802, USA
[11] Institute for Gravitation and the Cosmos, The Pennsylvania State University, University Park, PA 16802, USA
Received 2011 December 2; accepted 2012 May 3; published 2012 June 19

ABSTRACT

We provide a quantitative description and statistical interpretation of the optical continuum variability of quasars. The Sloan Digital Sky Survey (SDSS) has obtained repeated imaging in five UV-to-IR photometric bands for 33,881 spectroscopically confirmed quasars. About 10,000 quasars have an average of 60 observations in each band obtained over a decade along Stripe 82 (S82), whereas the remaining ∼25,000 have 2–3 observations due to scan overlaps. The observed time lags span the range from a day to almost 10 years, and constrain quasar variability at rest-frame time lags of up to 4 years, and at rest-frame wavelengths from 1000 Å to 6000 Å. We publicly release a user-friendly catalog of quasars from the SDSS Data Release 7 that have been observed at least twice in SDSS or once in both SDSS and the Palomar Observatory Sky Survey, and we use it to analyze the ensemble properties of quasar variability. Based on a damped random walk (DRW) model defined by a characteristic timescale and an asymptotic variability amplitude that scale with the luminosity, black hole mass, and rest wavelength for individual quasars calibrated in S82, we can fully explain the ensemble variability statistics of the non-S82 quasars such as the exponential distribution of large magnitude changes. All available data are consistent with the DRW model as a viable description of the optical continuum variability of quasars on timescales of ∼5–2000 days in the rest frame. We use these models to predict the incidence of quasar contamination in transient surveys such as those from the Palomar Transient Factory and Large Synoptic Survey Telescope.

Key word: quasars: general

Online-only material: color figures

1. INTRODUCTION

The optical continuum variability of quasars has been recognized since their first optical identification (Matthews & Sandage 1963), and it has been proposed and utilized as an efficient method for their discovery (van den Bergh et al. 1973; Hawkins 1983; Hawkins & Veron 1995; Ivezić et al. 2004a; Rengstorf et al. 2006). The observed characteristics of the variability can then be used to constrain the origin of their emission (e.g., Kawaguchi et al. 1998; Trevese et al. 2001, and references therein). The variability of quasars has typically been quantified using a structure function (SF) analysis (e.g., Hughes et al. 1992; Collier & Peterson 2001; Bauer et al. 2009; Kozłowski et al. 2010a; Welsh et al. 2011), where the SF is the root-mean-square (rms) magnitude change (Δm) as a function of the time lag (Δt) between measurements (similar to an autocorrelation function). It is fairly well established that quasar variability properties depend on physical properties such as the quasar luminosity, wavelength, timescale, and the presence of radio emission. However, despite considerable observational effort invested over last few decades, many conflicting claims about various correlations exist in the literature (see Giveon et al. 1999 for a detailed discussion).

The traditional method for studying variability has been to monitor a small, select sample of quasars over a long time baseline (e.g., Hawkins 2002; Giveon et al. 1999; Rengstorf et al. 2004). In this case, it is possible to compute the SF for each quasar, which can later be sample-averaged or studied individually. An alternative, utilized in more recent studies based on Sloan Digital Sky Survey (SDSS; York et al. 2000) and Palomar Observatory Sky Survey (POSS; Minkowski & Abell 1963) data, is to compute a single SF for all quasars in a particular wavelength or luminosity range. This approach, mandated by the fact that typically only a few epochs were available per object, only measures *ensemble* properties and *assumes* that all quasars selected from a narrow range of physical properties vary in the same way. Nevertheless, this approach enabled studies of quasar optical variability based on tens of thousands of objects and several hundred thousand photometric observations, as well as explorations of the long-term variability (Vanden Berk et al. 2004, hereafter VB04; Ivezić et al. 2004b, hereafter I04; Wilhite et al. 2005; Mahabal et al. 2005; De Vries et al. 2005, hereafter dV05; Sesar et al. 2006, hereafter Ses06). For example, the size and quality of the sample analyzed by VB04 (two-epoch photometry for 25,000 spectroscopically confirmed quasars) allowed them to

constrain how quasar variability in the rest-frame optical/UV regime depends upon rest-frame time lag (up to ∼2 years), luminosity, rest wavelength, redshift, the detection of radio or X-ray emission, and the presence of broad absorption line systems. By comparing SDSS and POSS measurements for ∼20,000 quasars spectroscopically confirmed by the SDSS, Ses06 constrained the optical quasar variability on timescales from 10 to 50 years (in the observer's frame). They report that there is a characteristic timescale of order 1 year in the quasar rest frame beyond which the SF flattens to a constant value. The SDSS has also facilitated both individual- and ensemble-based approaches by providing a large multi-epoch sample of quasars over the Northern Galactic Cap and well-sampled light curves in the Southern Stripe 82 (S82) survey. It is reassuring that the two approaches lead to similar SFs, as discussed by dV05. A test of this assumption is also described in MacLeod et al. (2008), who show that indeed the *mean* behavior is the same. With such large samples, the ensemble SF(Δt) slopes are well constrained, and the values suggest that accretion disk instabilities are the most likely mechanism causing the observed optical variability (VB04; Kawaguchi et al. 1998; see also Lyubarskii 1997). However, attempts to constrain physical models using the ensemble SF are invalid as soon as one realizes that the ensemble SF(Δt) is a weighted sum of individual quasars with different SFs (MacLeod et al. 2008).

While studies have traditionally examined "non-parametric" statistical measures of variability such as the SF, a major challenge has been to describe the variability of individual quasars in a compact way. Recently, the introduction of a damped random walk (DRW) model has provided a way to mathematically characterize quasar light curves in terms of a characteristic timescale (τ) and an amplitude (SF_∞), which are then correlated with the physical properties such as luminosity and black hole mass. Kelly et al. (2009, hereafter KBS09) modeled a sample of 100 quasar light curves as a DRW and suggested that thermal fluctuations driven by an underlying stochastic process such as a turbulent magnetic field may be the dominant cause for the optical flux fluctuations. Kozłowski et al. (2010b; hereafter Kozł10) applied the DRW model to the well-sampled Optical Gravitational Lensing Experiment (OGLE) light curves (Udalski et al. 1997, 2008) of mid-infrared-selected quasars behind the Magellanic Clouds from Kozłowski & Kochanek (2009). Their analysis shows that the DRW model is robust enough to efficiently select quasars from other variable sources, despite the large surface density of foreground Magellanic Cloud stars (see also Butler & Bloom 2011; MacLeod et al. 2011; Kozłowski et al. 2011).

In MacLeod et al. (2010, hereafter Mac10), we applied the DRW model to the light curves of ∼10,000 quasars in S82 and found a correlation between SF_∞ and black hole mass which is independent of the anticorrelations with luminosity and wavelength (see also Ai et al. 2010; Meusinger et al. 2011). We also found that τ increases with increasing wavelength, remains nearly constant with redshift and luminosity, and increases with increasing black hole mass (see also KBS09; Kozł10). In Kelly et al. (2011), it was shown that a similar stochastic model but with multiple timescales for a single object can accurately reproduce the X-ray variability of active galactic nuclei (AGNs) and microquasars. An inhomogeneous accretion disk model, where the temperature fluctuations throughout the disk are driven by a DRW process, can explain the disk sizes derived from microlensing light curves (see Morgan et al. 2010) while matching the observed level of optical variability, and predicts SEDs that are in better agreement with observations than standard thin disk models (Dexter & Agol 2011).

One defining feature of the DRW model for a *single* quasar is that it predicts a Gaussian distribution of magnitude differences Δm for a given Δt. On the other hand, the observed Δm distribution in the optical for an *ensemble* of quasars observed at two times separated by Δt deviates strongly from a Gaussian but is well fit by an exponential distribution (I04). This conflict represents an important puzzle for understanding the DRW model and its applicability to quasar light curves. Also, the high likelihood of extreme values of Δm has important implications for the interpretation of observations of transients. For example, Vanden Berk et al. (2002) reported the detection of an orphan gamma-ray burst afterglow based on the 2.5 mag decrease in optical flux. Such a large flux change was inconsistent with a quasar based on a Gaussian model for their variability, but the source was nevertheless confirmed to be a highly variable quasar (Gal-Yam et al. 2002). An accurate statistical description of the two-epoch photometry for ensembles of quasars will be important for transient detection in large surveys, where quasars represent a major contaminant.

Our goal here is to produce a unified view of ensemble and individual optical variability in the context of the DRW model. In this study, we show that the differences in shape between the ensemble SF and the DRW SF are well explained by averaging over the properties of individual quasars. We also show that the exponential distributions of magnitude changes for ensembles of quasars at fixed time lag are naturally constructed by summing the intrinsically Gaussian distributions of magnitude changes produced by individual quasars. There are several residual issues which we discuss as part of the comparison. An overview of the SDSS and POSS data used in this study is presented in Section 2. In Section 3, we describe the observed ensemble quasar variability in terms of the SF as a function of wavelength and time lag in the observer's frame. We then convert to rest-frame quantities and compare the data to a model ensemble SF based on our previous DRW analysis of S82 light curves. In Section 4, we combine the constraints on short-term quasar variability based on SDSS data with the constraints on long-term variability derived from matching the SDSS and POSS catalogs. In Section 5, we discuss the implications our results have on transient identification, with a focus on future time-domain surveys such as the Palomar Transient Factory (PTF) and the Large Synoptic Survey Telescope (LSST). Our results are discussed and summarized in Section 6.

2. DATA OVERVIEW

In this section, we briefly summarize the relevant SDSS and POSS data. We focus our description on the quasars with multiple observations (similar to MacLeod et al. 2010, 2011).

2.1. The Basic Characteristics of the SDSS Imaging Survey

The SDSS provides homogeneous and deep ($r < 22.5$) photometry in five passbands (u, g, r, i, and z; Fukugita et al. 1996; Gunn et al. 1998; Smith et al. 2002; Ivezić et al. 2004c) accurate to 0.02 mag, of up to 12,000 deg^2 in the Seventh Data Release (DR7; Abazajian et al. 2009). The DR7 sky coverage results in photometric measurements for about 357 million unique objects. Astrometric positions are accurate to better than 0.1 arcsec per coordinate (rms) for sources brighter than 20.5 mag (Pier et al. 2003), and the morphological information from the images allows robust star–galaxy separation to ∼21.5 mag (Lupton

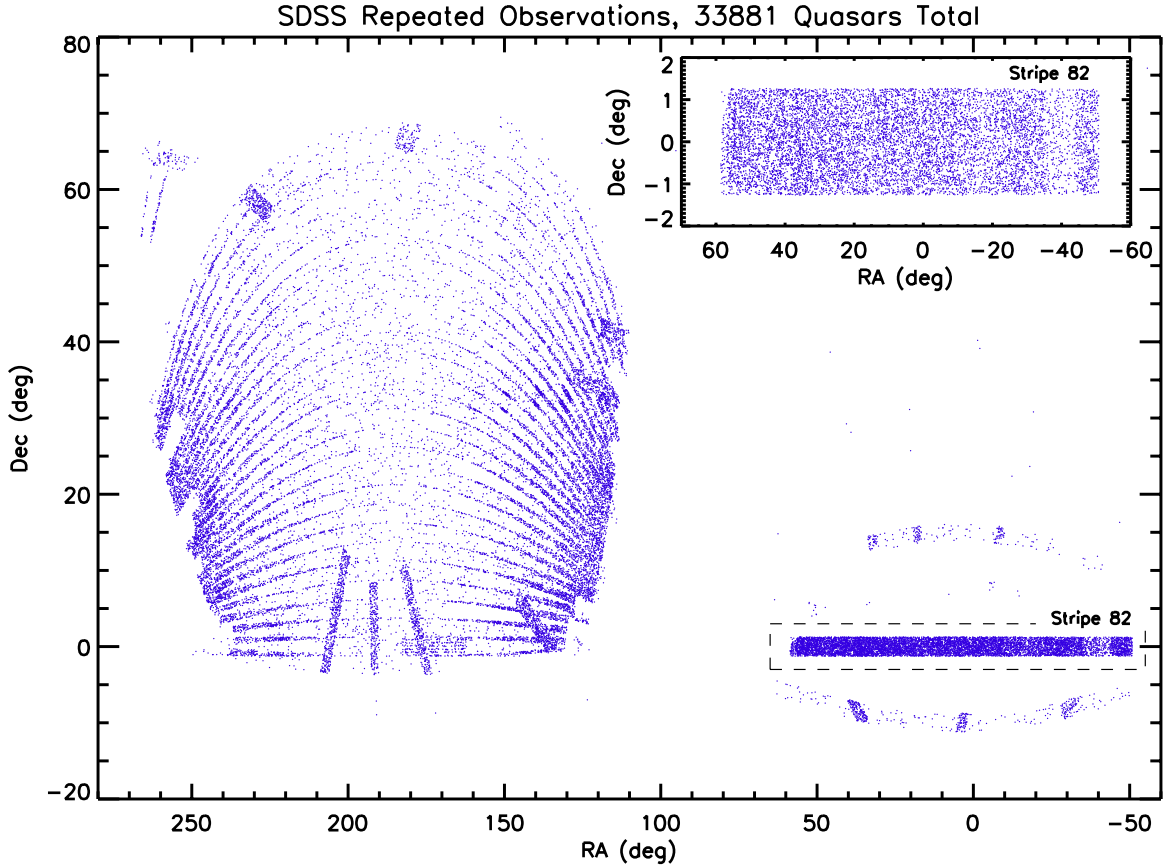

Figure 1. Distribution of 33,881 DR7 quasars with at least two observations on the sky in equatorial coordinates. The number of observations increases toward the survey poles where the "stripes" overlap. The inset shows a closer view of the SDSS Stripe 82, which has ∼60 observations per object (the density of quasars is non-uniform in S82 due to the increasing Galactic contribution toward negative R.A.).

(A color version of this figure is available in the online journal.)

et al. 2001). A compendium of technical details about the SDSS can be found in Stoughton et al. (2002).

The SDSS offers an unprecedented photometric accuracy for such a large-scale optical survey. Not only are the photometric errors generally small, but they are accurately determined by the photometric pipeline (*photo*; Lupton et al. 2001) and can be reliably used to estimate the statistical significance of measured magnitude differences. This ability is of paramount importance for a robust statistical study of variable objects. This error behavior is illustrated in Figure 2 in Ivezić et al. (2003). Throughout our analysis, we assume the SDSS photometric errors to be $\sigma_{\rm phot} = 0.018$ mag in g, r, and i bands, and 0.04 mag in u and z (see also Figure 1 in Sesar et al. 2007). The photometric errors are assumed to be independent of magnitude due to the bright sample limit of $i < 19.1$ (see the next section) and for simplicity when accounting for photometric errors in the SF calculations.

2.2. The SDSS Multi-epoch Data

The SDSS imaging data are obtained by imaging the sky in six parallel scanlines, each 13.5 arcmin wide (a "strip" in SDSS terminology). The six scanlines from two adjacent scans are then interleaved to make a filled "stripe." Because of the scan overlaps, and because the scans converge near the survey poles, ∼40% of the sky in the northern survey is essentially surveyed twice. In addition, 290 deg^2 of the southern survey area lies along S82 and has been observed about 60 times on average to search for variable objects and, by stacking the frames, to go deeper (Frieman et al. 2008; Annis et al. 2011). This valuable subsample contains well-sampled light curves for 9258 spectroscopically confirmed quasars whose variability properties are analyzed in Mac10, and it can be used to verify some of the results inferred from the analysis of two repeated observations. Overall, the SDSS has obtained multi-epoch data for ∼4000 deg^2 of sky, with timescales ranging from 2 hr to over 9 years, and with a wide range of Galactic latitudes extending all the way to the Galactic plane.

We define a quasar as any object listed in the SDSS catalog of spectroscopically confirmed quasars (the "DR7 Quasar Catalog;" Schneider et al. 2010). Its most recent fifth edition lists the SDSS DR7 BEST photometry for 105,783 quasars from 9380 deg^2. For a description of the spectroscopic target selection for quasars, see Richards et al. (2002). We note that the quality of photometry is good for the objects in the DR7 Quasar Catalog. In total, there are 33,881 spectroscopically confirmed quasars with at least two observations. We provide a catalog of all the SDSS repeated imaging of quasars online[12] (see the Appendix for a detailed catalog description). The sky distribution of repeatedly imaged quasars is shown in Figure 1.

When we compare pairs of observations, we use the secondary imaging observation with the largest time lag from the primary imaging observation listed in the DR7 Quasar Catalog, for a total of two observations per quasar. We define $\Delta m = m_2 - m_1$, where m_2 is the magnitude observed at a later epoch than m_1.

[12] http://www.astro.washington.edu/users/ivezic/macleod/qso_dr7/

We omit the S82 quasars since we do not wish to test our model on the same sample of objects from which the DRW model parameters were derived. The DR7 Quasar Catalog is spectroscopically complete to $i < 19.1$ in the quasar region of color space. Therefore, unless otherwise noted, we require that the primary observation for the remaining 24,627 quasars has $i \leqslant 19.1$ in order to be consistent with the flux limit of the quasar sample, for a total of 14,939 quasars. Given the SDSS limit of ∼22 mag, we further restrict the magnitude differences in each band to $|\Delta m| < 3$ mag in order to reduce the amount of contamination by poor photometry, for a total of ∼80,000 pairs of SDSS measurements (summed over all bands). Finally, we adopt the redshifts and absolute magnitudes listed in the Schneider et al. (2010) spectroscopic quasar catalog, and the black hole masses as measured from emission lines by Shen et al. (2011). All magnitudes are corrected for Galactic extinction using Schlegel et al. (1998).

2.3. SDSS–POSS Long-term Measurements

While SDSS S82 obtained measurements with time differences of up to 10 years, longer timescales of up to 50 years can be probed by comparing the SDSS and POSS catalogs. Ses06 have addressed the problem of large systematic errors in POSS photometry by recalibrating several publicly available POSS catalogs (USNO-A2.0, USNO-B1.0, DPOSS and GSC2.2). A piecewise recalibration of the POSS data in 100 arcmin^2 patches (one SDSS field) generally resulted in an improvement of photometric accuracy (rms) by nearly a factor of two compared to the original data (POSS-I magnitudes can be improved to ∼0.15 mag accuracy and POSS-II magnitudes to ∼0.10 mag accuracy). In addition to the smaller core width of the error distribution, the tails of the distribution become much steeper after the recalibration. These improvements are mostly due to the very dense grid of calibration stars provided by the SDSS, which rectifies the intrinsic inhomogeneities of Schmidt plates.

The much longer time lags between the Palomar Observatory Sky Surveys (POSS-I and POSS-II) and the SDSS (up to ∼50 years) than spanned by the available SDSS data make it easier to detect deviations of the SF from a simple power law. dV05 and Ses06 compared the SDSS and POSS data for over 10,000 quasars from the SDSS Data Release 2 in order to constrain the long-term quasar variability. As discussed by Ses06, the dV05 and Ses06 measurements of the SF agree within a 1σ uncertainty of the Ses06 measurements. Here, we use results from both the dV05 and Ses06 studies. We also make use of data from the Digitized Palomar Observatory Sky Survey (DPOSS; Djorgovski et al. 1998) that overlap 8000 deg^2 of sky from the SDSS Data Release 5. These DPOSS data were recalibrated following the procedure outlined by Ses06. There are 81,189 SDSS DR7 quasars with DPOSS observations in the G, R, and I bands, and we provide their two-epoch photometry at the same Web site (see footnote 12). For our analysis in Section 4, we use the primary SDSS observations as listed in the DR7 quasar catalog when comparing SDSS–DPOSS magnitudes. We calculate synthetic POSS GRI magnitudes from the SDSS photometry, require $i < 19.1$, and impose various quality cuts following Ses06. In total, we have 56,732 SDSS–DPOSS Δm measurements.

3. CHARACTERISTICS OF OBSERVED VARIABILITY

For our SF analysis, we examine the behavior in both the observer's and the quasar rest frames because the former is informative for data interpretation (e.g., transients in large surveys) and the latter constrains quasar physics. The SF behavior in the observer's frame is discussed in Section 3.1, and we convert to rest-frame quantities in Section 3.2. We handle various trends with observed properties by taking narrow ranges of the relevant quantities, in particular, the time lag and wavelength in each frame. The luminosity, mass, and redshift information are utilized in Section 3.2, where we test whether the scalings with these physical parameters derived from individual light curves in S82 can reproduce the ensemble variability of the two-epoch sample.

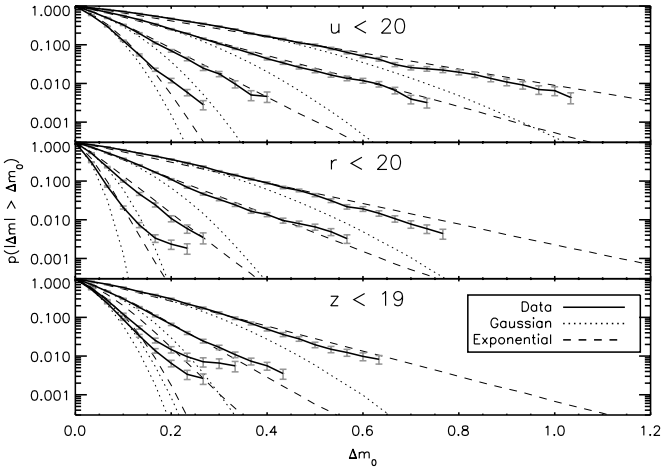

Figure 2. Observed cumulative distributions of urz magnitude differences as a function of time lag in the observer's frame. We define $\Delta m = m_2 - m_1$, where m_2 is the magnitude observed at an epoch later than m_1. The data (thick lines with Poissonian error bars) are only shown for sample sizes exceeding 10 data points (the probabilities become increasingly unreliable when below ∼0.003). Going from the narrowest distribution to the widest, the time lags span 1–30 days, 50–150 days, 200–400 days, and 1400–3000 days. The thin lines show the predicted distributions based on Gaussian (dotted) and exponential (dashed) analytic functions with the same rms as the data for each time lag range, where the photometric errors are taken into account by adding a Gaussian component of width $\sigma_{\rm phot}$ as defined in Section 2.1.

3.1. Quasar Variability in the Observer's Frame

Assuming that the observed variability reflects the physics in the accretion disk, the behavior in the observer's reference frame will be a convolution of rest-frame variability over redshift, luminosity, and other parameters. While this convolution will obscure important physical scalings, quasar variability in the observer's reference frame is still of major interest when interpreting survey data, in particular when distinguishing between quasars and other variable sources such as transients, or in using variability to select quasars. Therefore, we start by considering quasar variability in the observer's frame.

3.1.1. Δm Distribution

Figure 2 shows the cumulative distribution of Δm in the SDSS u, r, and z bands for four different Δt ranges. The thin lines show the predicted distributions based on Gaussian (dotted) and exponential (dashed) analytic functions with the same rms as the data. The photometric errors are taken into account by adding a Gaussian component of width $\sigma_{\rm phot} = 0.018$ mag in r and 0.04 mag in u and z. The exponential curves predict a much higher probability of large magnitude changes than the Gaussian curves, and the data follow this prediction (we only show the data for bins with more than 10 points). The data points become increasingly unreliable in the tails of each distribution

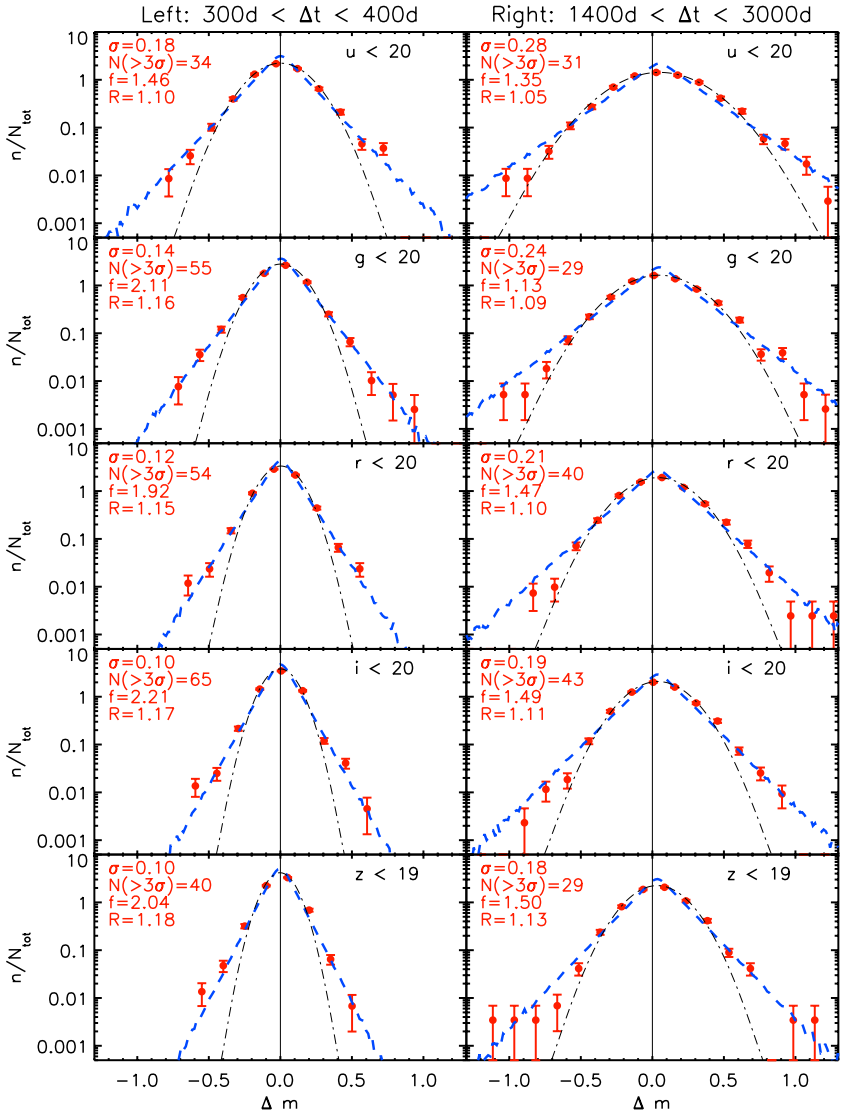

Figure 3. Symbols show the distribution of measured magnitude differences, Δm, in the five SDSS bands, and for two narrow ranges of time lag, Δt, as indicated at the top. n indicates the number of points in a bin divided by the bin width and $N_{\rm TOT}$ is the total number of points used for each histogram. The distribution width (σ) calculated using Equation (1), shown in each panel, is increasing with time and decreasing with wavelength. The dot-dashed lines show Gaussian distributions with a root mean square (rms) equal to σ, and the dashed lines show exponential distributions, $\exp(-\Delta m/\Delta_c)$, with $\Delta_c = {\rm rms}/\sqrt{2}$. Note that an exponential distribution provides a better fit to the wings of the observed distributions. Each panel also displays the number of measurements outside the $\pm 3\sigma$ range ($N > 3\sigma$), their corresponding fraction (f) expressed in percent (the expected value of this fraction for a Gaussian distribution is 0.3%, and for an exponential distribution 1.4%), and the ratio $R = {\rm rms}/\sigma$.

(A color version of this figure is available in the online journal.)

due to small sample sizes, and this fact may cause the large discrepancy with the exponential curve for small Δt in the r and z bands.

Figure 3 shows the differential Δm distributions for each SDSS band and for two slices of observed-frame time lag. The distribution width (i.e., the SF value) increases with time lag and decreases with wavelength. The wings of the distributions are also closer to exponential (more accurately, a double-exponential or Laplace distribution) than to Gaussian. Figure 4 shows similar distributions for the changes in color for two slices in time lag. The color changes are smaller than for the individual magnitudes at the same time separation. In the bottom six panels, the color changes are plotted against each other as well as against the r-band differences. Although the scatter around these relationships is quite large, quasars tend to get bluer as they brighten on average (bottom four panels), in accordance with previous results (e.g., Giveon et al. 1999). An analogous correlation was found recently by Schmidt et al. (2012), who analyzed individual light curves. Their study showed the slope s_{gr} between the r-band and g-band variations, as in $r - \langle r \rangle = (s_{gr}+1)(g - \langle g \rangle) + b$, is on average around -0.2, indicating that quasars get bluer as they brighten. This value corresponds to a slope of 4 in the bottom-right panel of Figure 4 (equating $m - \langle m \rangle$ to Δm), shown by the solid line, which approximately follows the observed, two-epoch distribution.

3.1.2. Structure Function

Next, we quantify the quasar variability using an SF analysis. Although several definitions can be found in the literature, the SF essentially measures the rms magnitude difference as a function of time lag between magnitude measurements. We compute the SF as

$$\mathrm{SF} = 0.74(\mathrm{IQR})/\sqrt{N-1}, \quad (1)$$

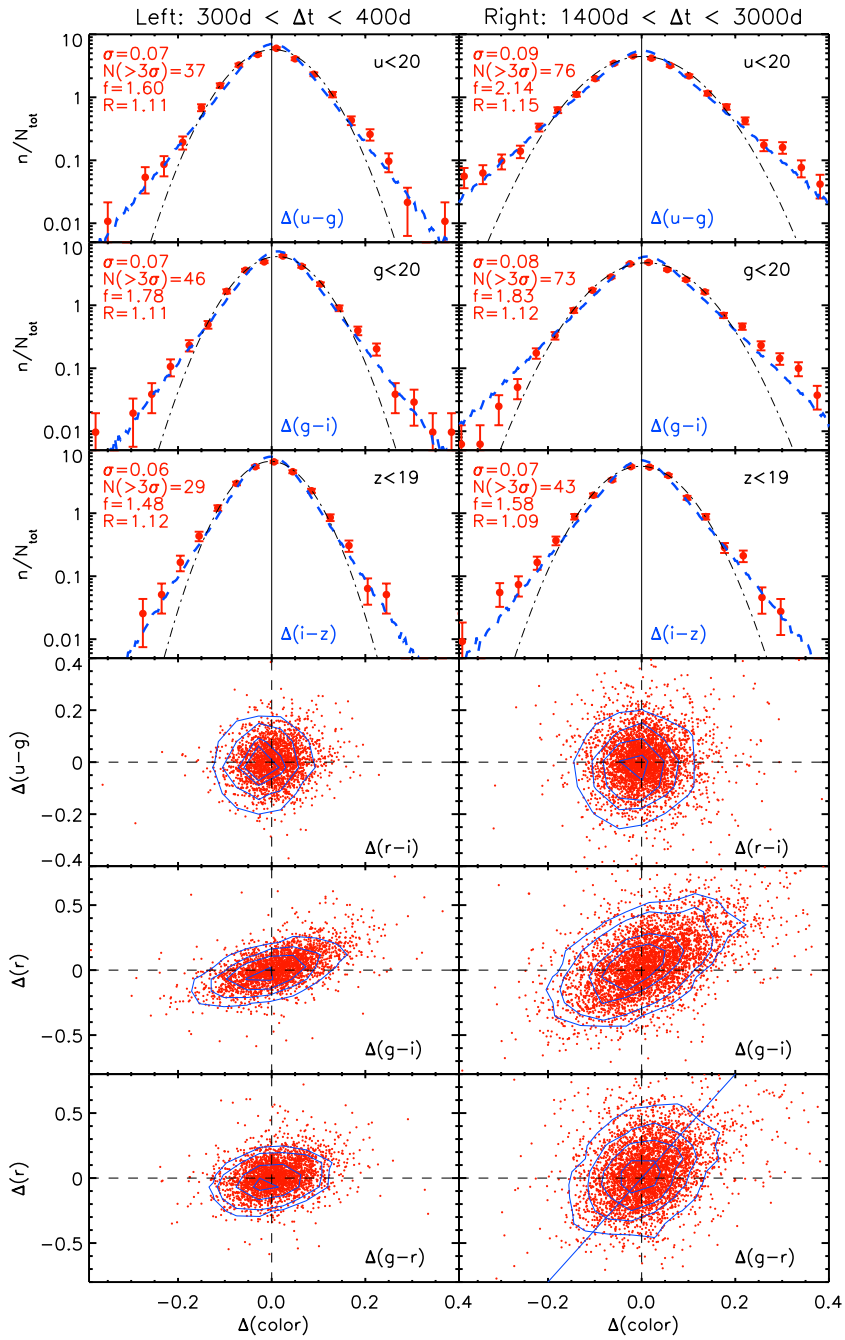

Figure 4. Top three rows are analogous to Figure 3, except that we show the changes in the $u-g$, $g-i$, and $i-z$ colors for two time lags in the observer's frame (left: 300–400 days and right: 1400–1600 days). The fourth row shows the change of $u-g$ color as a function of the change of $r-i$ color and the bottom two rows shows the change of the r-band magnitude as a function of the change of $g-i$ or $g-r$ color. The contours show regions containing 25%, 50%, 75%, and 90% of the data points. The solid line in the bottom-right panel shows the slope found by Schmidt et al. (2012) using individual quasar light curves.

(A color version of this figure is available in the online journal.)

where IQR is the 25%–75% interquartile range of the Δm distribution, and N is the number of Δm values. This approach is insensitive to outliers in the data which may result from poor data quality and is especially effective at short time lags where the SF is small. This value is equivalent to the rms if the distribution is Gaussian. When stated, the photometric errors are taken into account by subtracting $\sqrt{2}\sigma_{\rm phot}$ in quadrature from the SF. Two other definitions of the SF are found in the literature. Following Bauer et al. (2009), we refer to them as $\mathrm{SF}^{(A)}$ and $\mathrm{SF}^{(B)}$:

$$\mathrm{SF}^{(A)}(\Delta t) = \sqrt{\langle \Delta m^2 \rangle} \tag{2}$$

$$\mathrm{SF}^{(B)}(\Delta t) = \sqrt{\frac{\pi}{2}\,\langle |\Delta m| \rangle^2}. \tag{3}$$

For a Gaussian distribution, the ratio of the form adopted here to the other two forms is $\mathrm{SF}/\mathrm{SF}^{(A)} = \mathrm{SF}/\mathrm{SF}^{(B)} = 1$, while for an exponential (Laplace) distribution, $\mathrm{SF}/\mathrm{SF}^{(A)} = 1.03/\sqrt{2}$ and $\mathrm{SF}/\mathrm{SF}^{(B)} = 0.82$.

Figure 5 compares the SF for the combined SDSS and POSS data over timescales ranging from 5 days to 50 years in the observer's frame. The SF values shown up to $\Delta t \simeq 2000$ days are computed using Equation (1), with the photometric

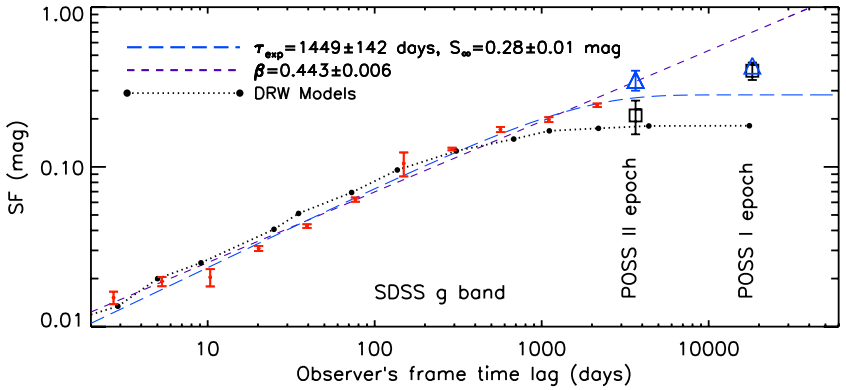

Figure 5. Structure function for quasar variability measured in the g band and in the observer's frame (corrected for errors using $\mathrm{SF} = \sqrt{\mathrm{SF}^2_{\mathrm{obs}} - 2\sigma^2_{\mathrm{phot}}}$). The red data points show the SDSS measurements, and the data points at $\Delta t > 3000$ days are inferred from comparing SDSS data and POSS I/II data, taken from Ses06 (open squares) and de Vries et al. (2003, blue triangles, which have similar errors as those from Ses06). The short-dashed line shows the best power-law fit to the SDSS measurements alone, $\mathrm{SF} \propto \Delta t^{\beta}$, and the long-dashed line shows a simultaneous fit to all data points, $\mathrm{SF} = S_\infty[1 - \exp(-\Delta t/\tau_{\mathrm{SF}})]^{1/2}$. The best-fit parameters for these two fits are listed in the upper-left corner. The dotted line shows the prediction of the DRW model trained on S82, as described in Section 3.2.1.

(A color version of this figure is available in the online journal.)

errors subtracted. For variability in the g band with time lags of 10 and 50 years, we adopt 0.35 and 0.43 mag to represent the dV05 results, and 0.21 and 0.40 mag for the Ses06 results, respectively. The errors in these estimates are ∼0.05–0.10 mag. The short-dashed line shows the best power-law fit to the SDSS measurements alone ($\mathrm{SF} \propto \Delta t^{0.44}$). It overestimates the variability level for timescales longer than several years. The long-dashed line shows the best-fit asymptotic function to all data points given by $S_\infty\,[1 - \exp(-\Delta t/\tau_{\mathrm{SF}})]^{1/2}$, a common parameterization of the SF (e.g., Hook et al. 1994), with S_∞ and τ_{SF} as free parameters. The limiting value of the best-fit overall SF, $S_\infty = 0.28 \pm 0.01$ mag, is probably systematically uncertain at a level of 0.02–0.03 mag due to the discrepancies between the SDSS–POSS-I/II measurements (see Ses06). The measured characteristic timescale, $\tau_{\mathrm{SF}} \sim 1400$ days, corresponds to ∼700 days in the rest frame and is uncertain by ∼10%–20%. While this analysis and the earlier ones by dV05 and Ses06 provide strong evidence that the SF levels out on long timescales, we cannot rule out a continuing but slower rise.

3.2. Quasar Variability in the Rest Frame

The redshift distribution of the quasars enables one to map a discrete distribution of wavelengths and time differences Δt in the observer's frame to a smoother distribution in the quasar rest frame. Figure 6 shows the distribution of our 79,787 Δm measurements for $i < 19.1$ objects in the rest-frame time difference (Δt_{RF}) and wavelength (λ_{RF}) plane. Most (54%) observations have $\Delta t_{\mathrm{RF}} < 50$ days. The discrete distribution[13] of λ_o and Δt_o in the observer's frame is spread along the lines $\Delta t_{\mathrm{RF}} = k\,\lambda_{\mathrm{RF}}$, with $k = \Delta t_o/\lambda_o$, and according to the sample redshift distribution [$\Delta t_{\mathrm{RF}} = \Delta t_o/(1+z)$, $\lambda_{\mathrm{RF}} = \lambda_o/(1+z)$]. Here, we consider the shape of the Δm distribution as a function of these quantities, the form of $\mathrm{SF}(\Delta t_{\mathrm{RF}})$, and the dependence of the SF on all physical parameters simultaneously, including the i-band absolute magnitude M_i (K-corrected to the rest frame) and the black hole mass M_{BH}.

3.2.1. Application of a DRW Model

We develop a model SF that reproduces the observed ensemble variability using information derived from individual quasar light curves in S82. Our model is motivated by the success of a DRW in describing quasar light curves (KBS09; Kozł10; Mac10), as well as the detection of a turnover in the ensemble SF on long timescales, suggesting a characteristic timescale for variability (e.g., Ses06; Welsh et al. 2011). We assume that the turnover is a consequence of the characteristic timescale distribution measured among individual quasars, and that the turnover in the ensemble SF corresponds to the average timescale, τ_{SF}. Suppose each quasar is described by its own DRW parameters, τ and SF_∞. Then, the ensemble SF is a weighted contribution of all the individual SFs over their distribution in these parameters,

$$\mathrm{SF}(\Delta t) = \int d\tau\, d\mathrm{SF}_\infty \frac{d^2n}{d\tau\, d\mathrm{SF}_\infty} \mathrm{SF}(\Delta t|\tau, \mathrm{SF}_\infty)_{\mathrm{qso}}, \quad (4)$$

where $\mathrm{SF}(\Delta t|\tau, \mathrm{SF}_\infty)_{\mathrm{qso}}$ is the SF at time Δt for a quasar with DRW variability parameters τ and SF_∞, given by

$$\mathrm{SF}(\Delta t|\tau, \mathrm{SF}_\infty)_{\mathrm{qso}} = \mathrm{SF}_\infty(1 - e^{-|\Delta t|/\tau})^{1/2}. \quad (5)$$

In particular, $\mathrm{SF}(\Delta t)_{\mathrm{qso}}$ is the expected standard deviation of magnitude differences Δm for a given quasar at a time lag Δt. $\mathrm{SF}(\Delta t)_{\mathrm{qso}}$ is related to the standard deviation in magnitudes (σ_m) at a given Δt by $\mathrm{SF}(\Delta t)_{\mathrm{qso}} = \sqrt{2}\sigma_m$, where the factor of $\sqrt{2}$ results from subtracting two magnitudes.

To build a model for the ensemble variability, we follow these steps for each quasar in the two-epoch sample.

1. Predict τ and SF_∞ based on the quasar's physical parameters.
2. Include the intrinsic scatter in τ and SF_∞ for quasars with similar physical parameters.
3. Estimate the SF value at the measured time lag Δt_{RF} using Equation (5).
4. Draw one model Δm value from a Gaussian distribution with a width set by $\mathrm{SF}(\Delta t_{\mathrm{RF}})_{\mathrm{qso}}$, adding photometric noise if necessary.

[13] Note that a discretely distributed observed Δt can lead to artificial correlations between the SF and Δt_{RF}. For fixed Δt_o, longer Δt_{RF} correspond to both lower redshift and, because of magnitude limits, lower luminosities. Since there is also an anticorrelation between variability amplitude and luminosity, this leads to an SF that increases toward higher Δt_{RF}. Therefore, caution must be taken when binning in Δt_{RF} using very sparse Δt_o so that one does not mistake wiggles in the ensemble $\mathrm{SF}(\Delta t_{\mathrm{RF}})$ for multiple intrinsic timescales, for example.

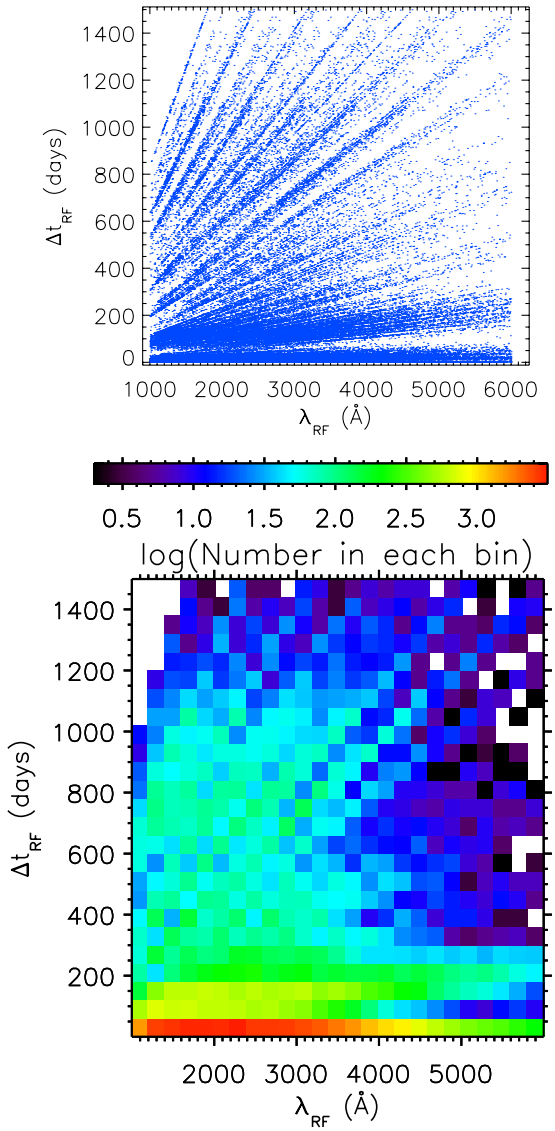

Figure 6. Top: the distribution of SDSS magnitude difference measurements in the plane spanned by rest-frame wavelength, $\lambda_{\rm RF}$, and time lag, $\Delta t_{\rm RF}$. The discrete distribution of λ_o and Δt_o in the observer's frame is spread along the lines $\Delta t_{\rm RF} = k\,\lambda_{\rm RF}$, with $k = \Delta t_o/\lambda_o$, and according to the sample redshift distribution [$\Delta t_{\rm RF} = \Delta t_o/(1+z)$, $\lambda_{\rm RF} = \lambda_o/(1+z)$]. The bottom panel shows the number of measurements in each bin on a log scale according to the legend at top. The white pixels contain fewer than five data points.

(A color version of this figure is available in the online journal.)

We generally average over 1000 of these Monte Carlo models for the distributions expected from the DRW model.

In the first step, τ and SF_∞ are estimated using the scalings of the DRW parameters with the quasar's physical parameters found in Mac10:

$$\log f = A + B\log\left(\frac{\lambda_{\rm RF}}{4000\,\text{Å}}\right) + C(M_i + 23) + D\log\left(\frac{M_{\rm BH}}{10^9\,M_\odot}\right) + E\log(1+z), \quad (6)$$

where $A = -0.51$, $B = -0.479$, $C = 0.131$, and $D = 0.18$ for $f = \mathrm{SF}_\infty$ (in mag), and $A = 2.4$, $B = 0.17$, $C = 0.03$, and $D = 0.21$ for $f = \tau$ (in days). Note that the dependence on redshift was found to be negligible in both cases ($E = 0$). By applying this model to the quasars in the large two-epoch sample, we are also testing the accuracy of the scalings derived for the S82 quasars.

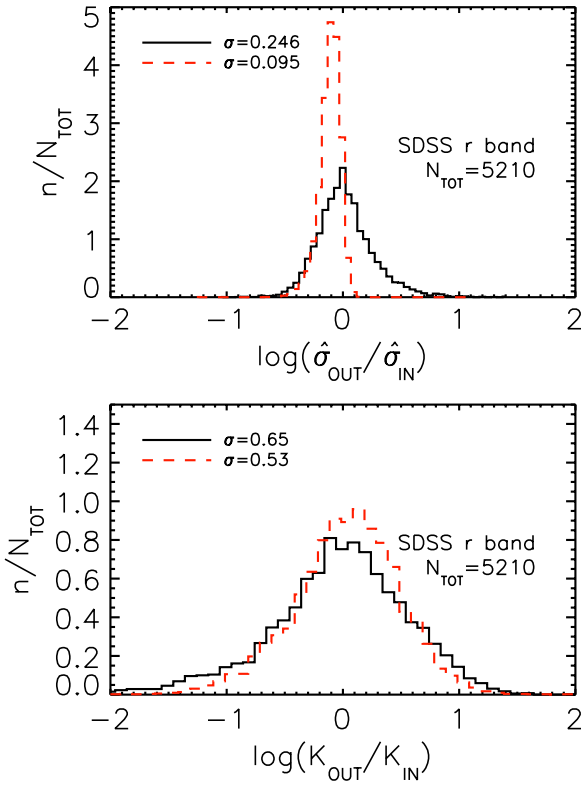

Figure 7. Determination of fitting errors. The distributions of DRW parameters $\hat{\sigma} = \mathrm{SF}_\infty/\sqrt{\tau}$ and $K = \tau\sqrt{\mathrm{SF}_\infty}$ for Monte Carlo models of S82 quasar light curves are shown in the top and bottom panels, respectively. The solid, black curve in each panel shows the distribution of observed $\hat{\sigma}$ (K) values, which are used as inputs to generate the light curves, normalized by the median value of 0.16 mag yr$^{-1/2}$ (200 mag$^{1/2}$ days). The red, dashed line shows the ratio between the best-fit parameters for the simulated light curves and their input values. The red histogram is narrower than the black histogram since the resulting best fit should be similar to the input value that generated the light curve. The contribution of fitting errors to the overall scatter of observed values is estimated to be the ratio of the variances (σ^2) of the red and black histograms.

(A color version of this figure is available in the online journal.)

In the second step, we account for the intrinsic scatter in τ and SF_∞ for quasars with similar physical parameters. When measured for individual quasar light curves, τ and SF_∞ show scatter about their mean trends (Equation (6)). The magnitudes of these residuals are too large to be fully attributed to measurement uncertainties (Mac10; Bauer et al. 2011). From simulations (see Section 4.2 of Mac10), we estimated that the latter statistical uncertainties account for only 70%, 60%, and 13% of the scatter in τ, SF_∞, and $\hat{\sigma} = \mathrm{SF}_\infty/\sqrt{\tau}$, respectively. The fitting errors are much smaller for $\hat{\sigma}$ because it is well constrained even for light curve lengths shorter than τ. If we define $K = \tau\sqrt{\mathrm{SF}_\infty}$ as a variable orthogonal to $\hat{\sigma}$ (in log space), its uncertainty due to fitting errors contributes ~82% of its scatter. Figure 7 compares the scatters in observed $\hat{\sigma}$ (top panel) and K (bottom panel) for S82 quasars to those for Monte Carlo models of the light curves.

Figure 8 shows the distributions of $\hat{\sigma}$ and K measured for the S82 sample compared to their expected values from Equation (6). We find that the differences between the observed $\log\hat{\sigma}$ ($\log K$) and the estimates from Equation (6) peak near zero with an rms of 0.16 (0.62) dex. After taking the fitting errors into account, the rms is reduced to 0.149 (0.26) dex, which we take as the intrinsic stochasticity. Therefore, in the second step,

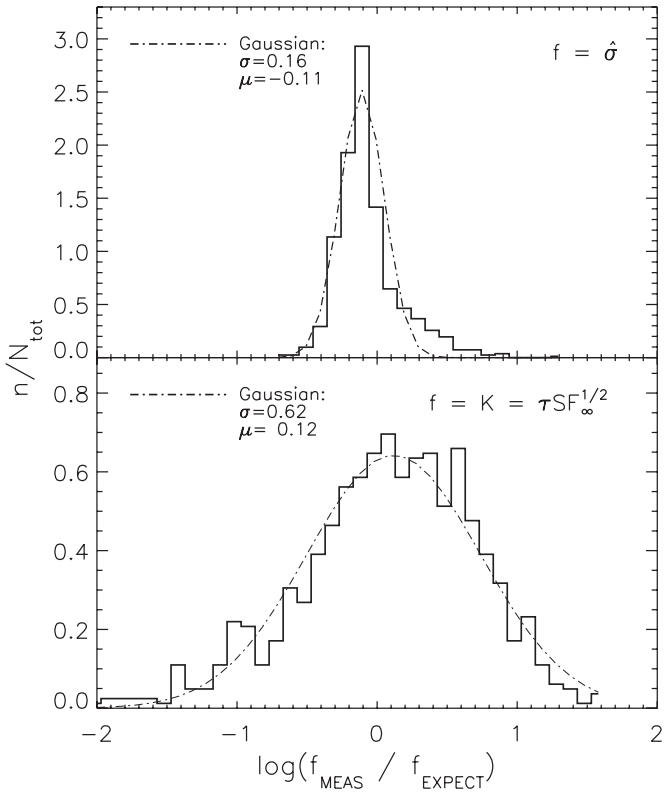

Figure 8. Distributions of $\hat{\sigma} = \mathrm{SF}_\infty/\sqrt{\tau}$ and $K = \tau\sqrt{\mathrm{SF}_\infty}$ for S82 quasar light curves with $r < 19$, normalized by the expected values from Equation (6). Each dot-dashed curve shows a Gaussian with unit area, with a mean (μ) and rms (σ) as listed in the legends. After removing the contribution from fitting errors ($F = 13\%$ and 82% for $\hat{\sigma}$ and K, respectively), the intrinsic distribution widths are $\sigma_{\rm int} = 0.149$ and 0.26 dex, where $\sigma_{\rm int} = (\sigma^2 - F\sigma^2/100)^{1/2}$.

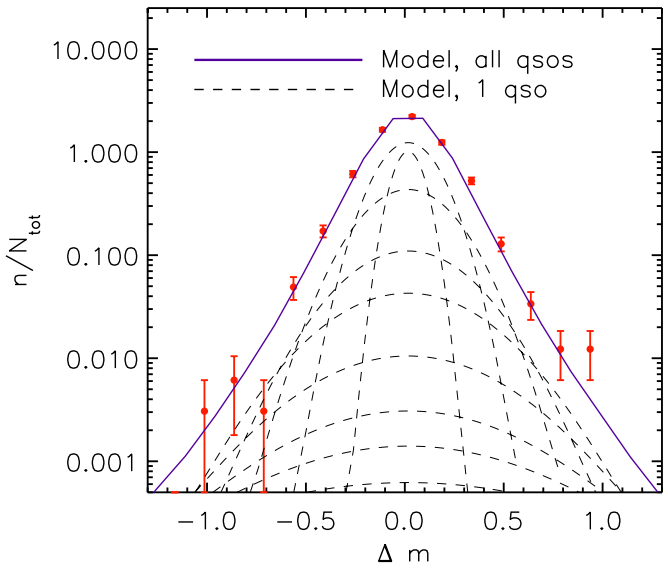

Figure 9. Red data points with errors bars show the observed magnitude difference distribution for 365 days $< \Delta t_{\rm RF} <$ 730 days and 2000 Å $< \lambda_{\rm RF} <$ 3000 Å. The solid line shows the expected distribution based on the DRW model. The dashed Gaussian curves show the expected distributions for nine individual quasars with different values of $\mathrm{SF}(\Delta t_{\rm RF})_{\rm qso}$ (and thus τ and SF_∞; see Equation (5)). Each curve has been convolved with a Gaussian noise component of width $\sigma_{\rm phot}$ to account for photometric errors, and shifted by the median of the observed distribution.

(A color version of this figure is available in the online journal.)

we take the τ and SF_∞ estimated from Equation (6), compute $\hat{\sigma}$ and K, add a random Gaussian deviate of width 0.149 (0.26) dex to each $\log\hat{\sigma}$ ($\log K$) value, and then convert back to τ and SF_∞. This process should provide a reasonable model for the intrinsic scatter.

In the third step, the SF for a particular quasar at a given $\Delta t_{\rm RF}$ is estimated using Equation (5). In the fourth step, a model Δm value is drawn from a Gaussian distribution with a standard deviation of $\mathrm{SF}(\Delta t_{\rm RF})_{\rm qso}$, the Gaussian distribution expected from the DRW model. To account for photometric errors, we further add a random Gaussian deviate of width $\sqrt{2}\sigma_{\rm phot}$ to each model Δm value (the $\sqrt{2}$ factor results from adding the photometric errors in quadrature). This procedure results in one model Δm value per quasar based on the expectations from the DRW model. We then repeat this 1000 times for each quasar in the sample. The resulting model for the ensemble SF is then the rms width of this model Δm distribution otherwise calculated in the same way as for the data (using the interquartile range).

3.2.2. Explaining the Exponential Tails of the Δm Distribution

In Figure 9, the observed magnitude difference distribution is shown for a narrow slice in $\Delta t_{\rm RF}$ and $\lambda_{\rm RF}$. The observed distribution is very similar to the model distribution (solid line), in which each quasar is assigned a model Δm value drawn from a particular $\mathrm{SF}(\Delta t_{\rm RF})_{\rm qso}$, as described above. The exponential distribution for large $|\Delta m|$ results from a superposition of many Gaussians (dashed lines) corresponding to different values of $\mathrm{SF}(\Delta t_{\rm RF})_{\rm qso}$. The range in $\mathrm{SF}(\Delta t_{\rm RF})_{\rm qso}$ is caused by differing τ and SF_∞ values, which can be attributed to a range in quasar luminosity and black hole mass plus intrinsic scatter.

Figure 10 shows the distribution of Δm in four bins of rest wavelength and three bins of rest-frame time lag. The distributions remain exponential at large $|\Delta m|$ for all 12 combinations of $\Delta t_{\rm RF}$ and $\lambda_{\rm RF}$, as illustrated by the dashed lines. The model distributions, which carry information about each individual quasar's expected DRW parameters (and thus incorporate the M_i and $M_{\rm BH}$ information), are shown as solid curves. The observed and predicted $\mathrm{SF}(\Delta t_{\rm RF})_{\rm qso}$ values (σ) are listed to the right and left of each histogram, respectively. The model and data distributions agree well, showing that *the exponential distributions seen in the statistics of ensembles of quasars naturally result from averaging over quasars that are individually well described by a Gaussian DRW process.* There are two systematic discrepancies, however. First, while the exponential tails can be reproduced at large rest-frame time lags ($500 < \Delta t_{\rm RF} < 1500$ days), the value of the observed SF is systematically higher. Since there are no known intrinsic differences in the physical properties of the S82 quasars and the two-epoch sample studied here, the discrepancy is likely due to biases in estimates of the DRW variability parameters for the S82 quasars. Second, at small time lags ($50 < \Delta t_{\rm RF} < 150$ days), the model overpredicts the data rms by 10%, while the statistical uncertainty is 1% assuming a perfect Gaussian distribution of Δm and no other systematic errors. This discrepancy may be due to some systematic effect that was not accounted for when computing the error bars (or when correcting for the SDSS photometric errors). Alternatively, the discrepancy could result if the DRW model is inaccurate on these timescales (1–200 days). These discrepancies are discussed further in Section 4.1.

3.2.3. The SF as a Function of Time Lag and Wavelength

Now that we understand and can reproduce the shape of the distribution of magnitude changes Δm between two times,

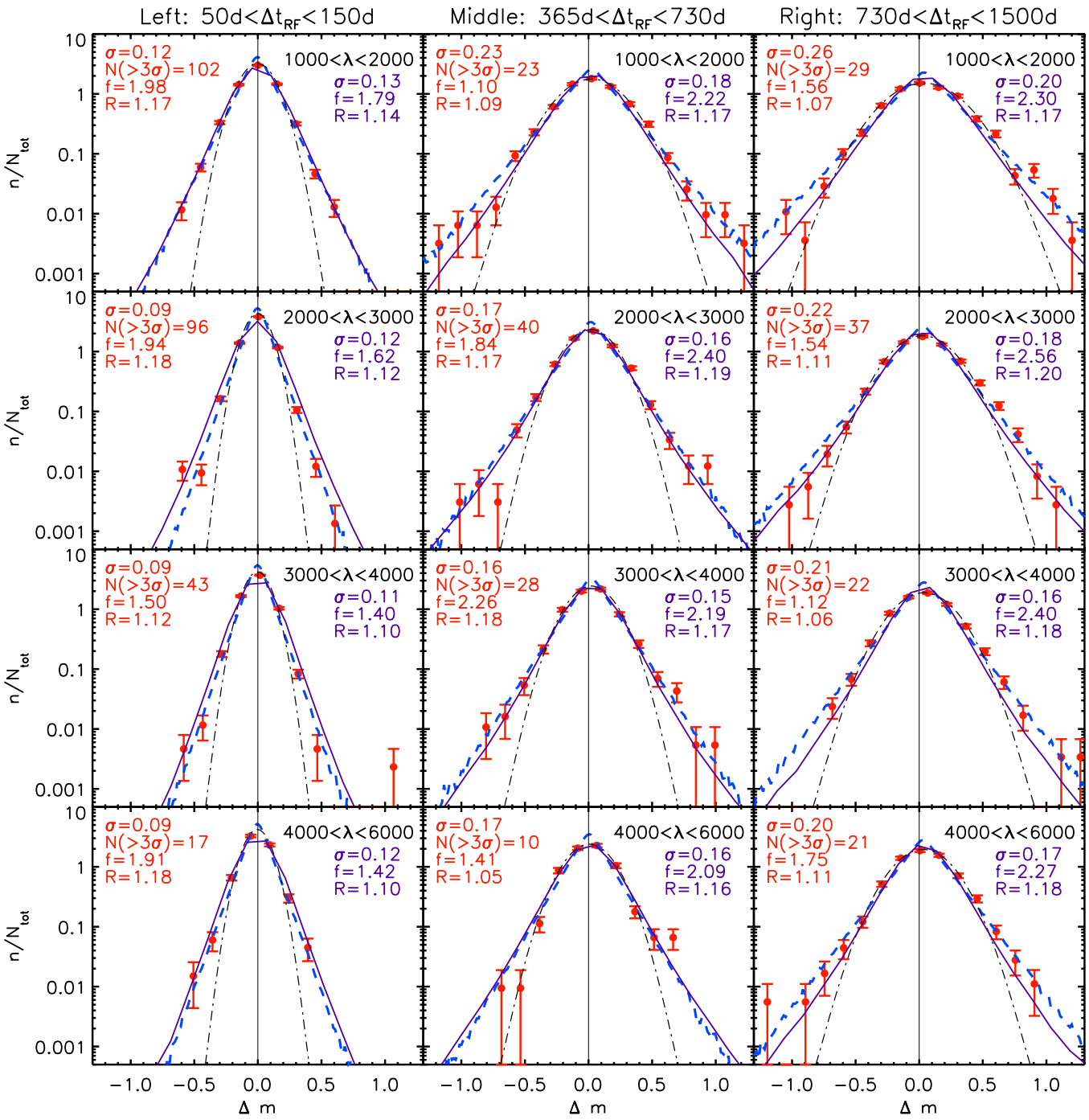

Figure 10. As in Figure 3, except that the symbols show the distribution of measured magnitude differences, Δm, for subsamples selected using rest-frame quantities, as marked in the panels. Each row corresponds to the same wavelength range and each column to the same $\Delta t_{\rm RF}$ range. The solid lines show the predicted DRW model distributions (see Section 3.2.1) with widths σ listed to the right of the histograms.

(A color version of this figure is available in the online journal.)

we can simply consider the SF (i.e., the width of this Δm distribution) as a function of physical quantities such as $\Delta t_{\rm RF}$ and $\lambda_{\rm RF}$ and test the model prediction. Figure 11 shows the SF as a function of $\Delta t_{\rm RF}$. Here, the measured SF is not corrected for the SDSS photometric accuracy. Again, it is apparent that the model predicts a systematically lower SF for time lags less than 200 days. However, the stochastic model predicts a systematically higher SF for the longest time lags. This suggests the model SF may be biased low at long time lags, and the bias seems to be most prominent at shorter wavelengths (Figure 12). Note that the measurements at long rest-frame time lags and short rest wavelengths are dominated by the u band, so there may be biases simply from the fact that the 14% of u and z light curves which were dominated by noise were omitted from the analysis in Mac10. We investigate such biases further in Section 4.1.

In Figure 13, we show the observed ensemble SF without correction for the SDSS photometric errors. We also show the signal-to-noise ratio for each bin (top-right panel). In the bottom-left panel, we show the model expectation including the estimated photometric errors. The bottom-right panel shows the (data–model) residuals. Overall, the results are excellent,

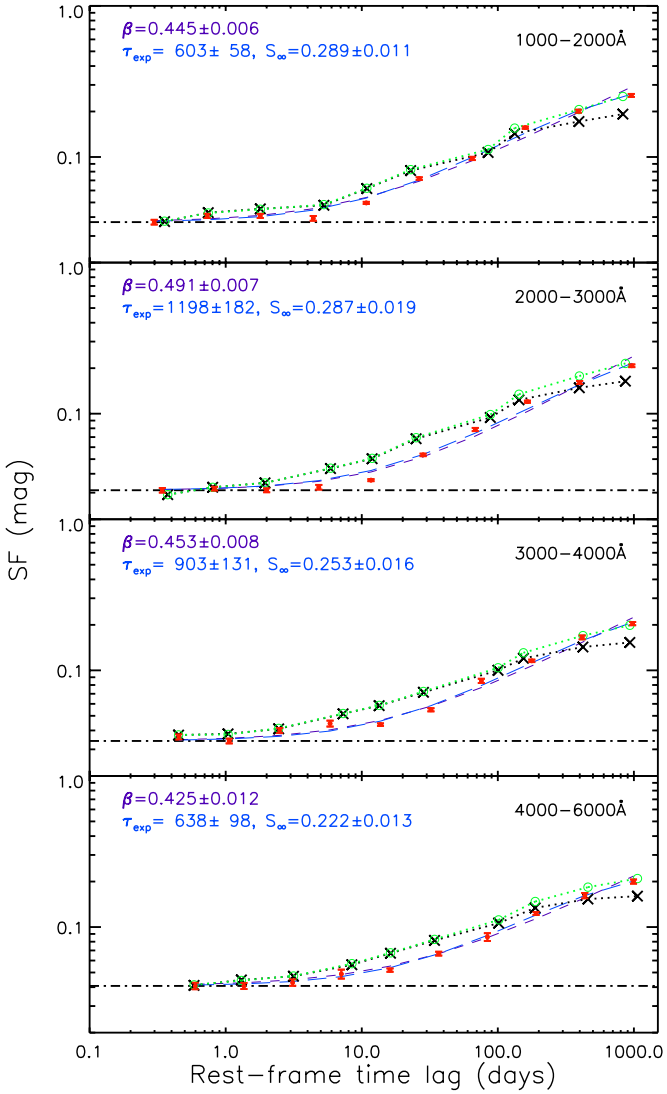

Figure 11. Red symbols show the structure function for quasar variability as a function of rest-frame time lag, for four ranges of rest-frame wavelength, as marked. The short-dashed line in each panel is the best-fit power law (SF $\propto \Delta t^{\beta}$), with β marked in each panel. The long-dashed lines are the best-fit exponential curves, SF $= S_{\infty}[1-\exp(-\Delta t/\tau_{\rm SF})]^{1/2}$, with the parameters listed in each panel. Both curves include a photometric noise component equal to the minimum measured SF in each panel (marked by the horizontal dot-dashed line). The dotted lines with cross symbols show the DRW model prediction (for 100 realizations, see Section 3.2.1). The green dotted lines with circles show the prediction of the DRW model trained on S82 data with all τ and SF$_{\infty}$ values multiplied by 2 and $\sqrt{2}$, respectively.

(A color version of this figure is available in the online journal.)

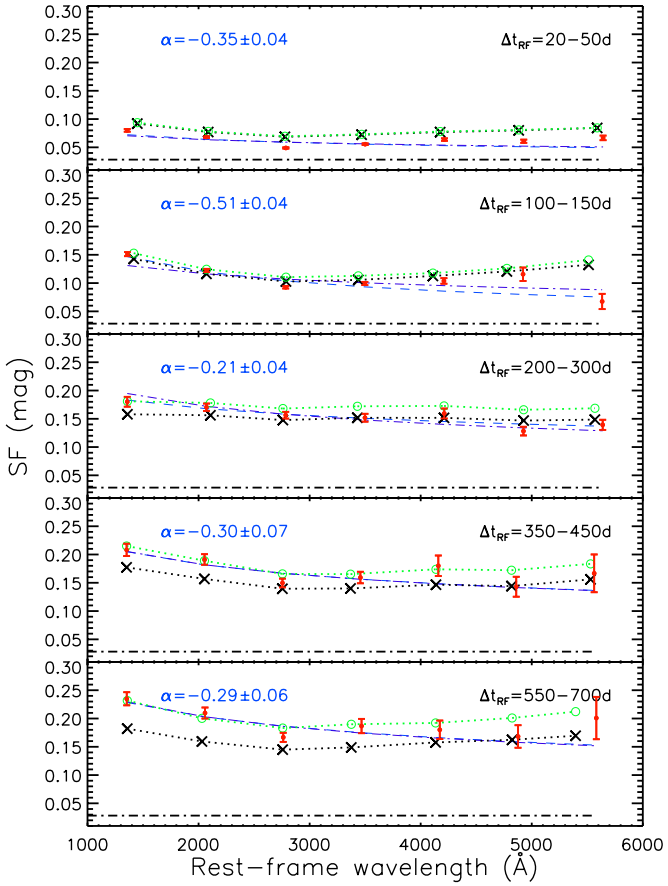

Figure 12. Red symbols show the structure function for quasar variability as a function of rest-frame wavelength, for five ranges of rest-frame time lag, as marked. The dashed lines are the best-fit power laws (SF $\propto \lambda^{\alpha}$) with the power-law index listed in the top-left corners. The dash-dotted lines show the functional dependence adopted by I04 ($\alpha = -0.3$). Both curves include a photometric noise component corresponding to $\sigma_{\rm phot} = 0.02$ mag. The dotted lines with cross symbols show the DRW model prediction (for 100 realizations, see Section 3.2.1). The green dotted lines with circles show the prediction of the DRW model trained on S82 data with all τ and SF$_{\infty}$ values multiplied by 2 and $\sqrt{2}$, respectively.

(A color version of this figure is available in the online journal.)

with a median difference of only 0.02 mag and a median absolute difference of 0.03 mag. We see a slight decrement at $\Delta t < 200$ days in the residuals at wavelengths coincident with the 2800 Å Mg II emission line. This decrement is expected based on the results of Reichert et al. (1994), where the Mg II emission line is less variable and lags the continuum fluctuations by almost 10 days. In Figure 14, the time axis is collapsed onto the wavelength axis (using the weighted mean) so that the dip in the residuals is emphasized. Due to the excellent SDSS photometry and large sample size, we are able to resolve this feature. Note that the large width of the decrement may be due to the fact that the rest wavelengths are approximated from the fixed effective wavelengths of the SDSS bands. Not accounting for the variation of the effective wavelength with the shape and redshift of the quasar spectrum sampled limits the accuracy of the approximated rest wavelengths. Thus, any line feature will be weakened and smoothed by the broad bandpasses of the SDSS filters.

4. COMBINING SHORT- AND LONG-TERM QUASAR VARIABILITY MEASUREMENTS (SDSS–POSS)

The exponential distribution analysis in Section 3.2 is sensitive to both SF$_{\infty}$ and τ through the better determined combination defined by $\hat{\sigma} = {\rm SF}_{\infty}/\sqrt{\tau}$. However, for the long-term SDSS–POSS data, the Δm distribution is mainly sensitive to SF$_{\infty}$ or τ at fixed $\hat{\sigma}$. It is then of interest to see whether the Δm distribution remains exponential at large $|\Delta m|$ and if we can reproduce the ensemble SF(Δt) on these long timescales. Therefore, we repeat the analysis in Section 3.2 using the 81,189 SDSS quasars that are also observed in DPOSS. We only use the DPOSS data for the Δm analysis because the errors for POSS-I are significantly larger. After applying the data quality cuts, there are 56,732 total Δm measurements in the G, R, and I bands. Figure 15 shows the distribution of time lags in the observed and rest frames.

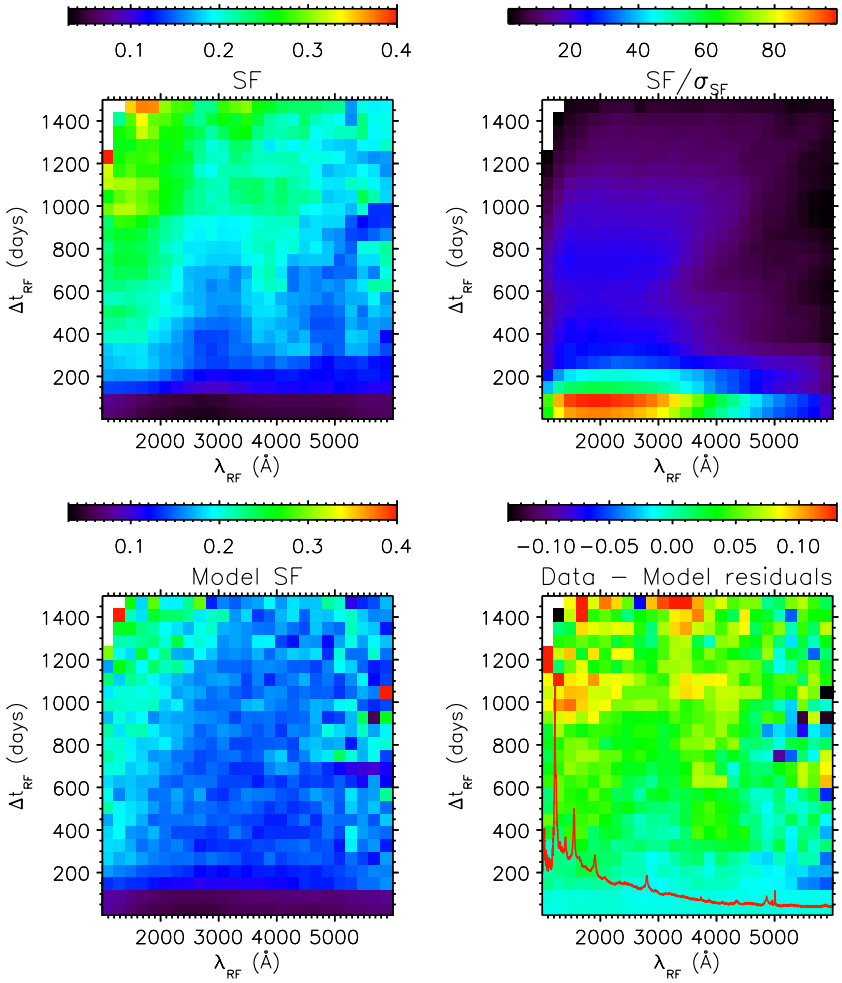

Figure 13. Top-left panel displays the structure function for quasar variability measured by the SDSS as a function of rest-frame wavelength and time lag. SF is computed as $0.74(\mathrm{IQR})/\sqrt{N-1}$, where IQR is the 25%–75% interquartile range. The figure is based on 79,787 SDSS measurements, and shows the structure function on a linear scale from 0.03 to 0.4 mag, as indicated in the top bar. The top-right panel shows the SF signal to noise, where the error σ_{SF} is computed as $1.15\mathrm{SF}/\sqrt{N-1}$. The bottom-left panel shows the model structure function (see the text), and the bottom-right panel shows the (data–model) residuals. The red line shows the SDSS composite quasar spectrum in arbitrary flux (F_λ) units from Vanden Berk et al. (2001). The weak vertical feature in the residual map at ∼2800 Å is coincident with the Mg II line visible in the composite spectrum. The white pixels in each panel contain fewer than five data points even when including all adjacent bins (and thus are not used in our analysis).

(A color version of this figure is available in the online journal.)

The SDSS–DPOSS Δm distributions are shown in Figure 16. Due to the larger photometric errors, these distributions appear more Gaussian than those restricted to SDSS observations. In some panels, the peak is also offset from zero toward positive Δm values. This is likely due to the Malmquist-like bias discussed in dV05, where many objects that were fainter at the time of the DPOSS observation were then lost and not included. In general, the model curves (solid lines) are able to reproduce the shape of the distributions but underestimate the rms, even when accounting for the estimated photometric errors of $\sigma_{\mathrm{phot}} = 0.1$ mag.

Finally, Figure 17 shows the SF over a large range of rest-frame time lag, including the SDSS–POSS data as measured in Ses06. We find an overall characteristic timescale of 835 ± 82 days with $\mathrm{SF}_\infty = 0.26 \pm 0.01$ mag. Note that in dV05, the SF reaches 0.46 ± 0.02 mag at 40 years in the rest frame for the g and r bands combined.

4.1. Data–Model Comparison

In Figure 17, we show our model SF as described in Section 3.2.1. We again see that the model is biased to higher values of the SF between 1 and 200 days. We attribute this discrepancy to one or both of the following.

1. At short Δt, the errors in our measured SF are underestimated, and some source of systematic error, such as an inaccurate correction for SDSS photometric errors, causes the measured SF to appear smaller than what the model predicts.
2. The DRW model is inaccurate at short Δt and therefore overpredicts the ensemble SF. However, this is unlikely given that the results using S82 light curves as well as densely sampled OGLE light curves (Zu et al. 2012) show the DRW model to be a good fit on timescales between ∼5 and 200 days.

Nevertheless, our measured slope of the SF seems well constrained. We again see that beyond 200 days, the model is biased to lower values of the SF. The difficulty to exactly reproduce the long-term variability amplitudes suggests that the distributions of long-term amplitudes and/or timescales used in our model underestimate the true distributions. This bias may result from the following.

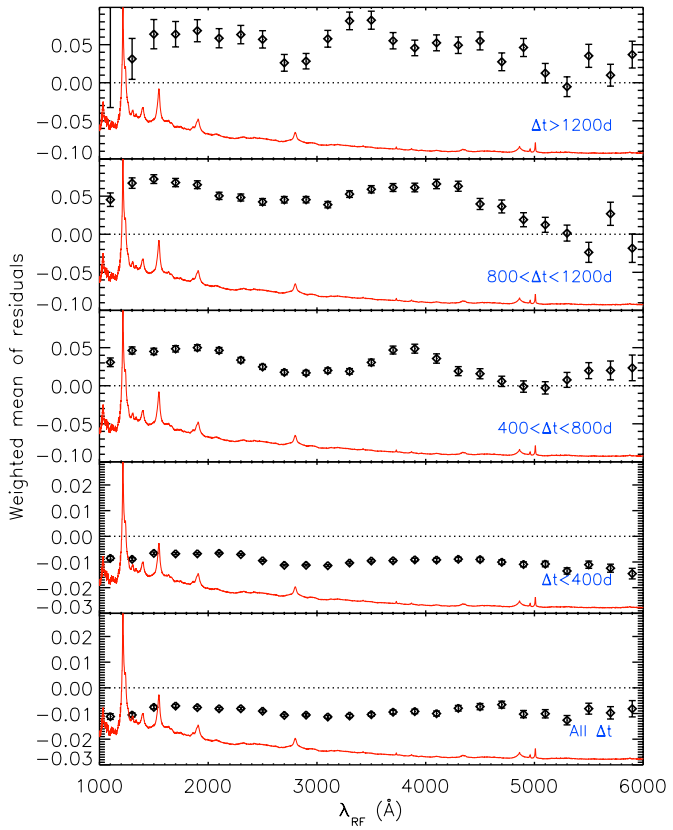

Figure 14. Weighted mean of the data–model residuals as a function of rest wavelength (the bottom-right panel of Figure 13 collapsed onto the wavelength axis). The weighted mean of all time lag bins i is defined as $\sum(\mathrm{SF}_i - \mathrm{SF}_{\mathrm{model},i})w_i / \sum w_i$, where $w_i = 1/\sigma^2_{\mathrm{SF}}$, the uncertainty from Figure 13. The error bars of the weighted means are computed as $(\sum w_i)^{-1/2}$. The composite quasar spectrum is overplotted in arbitrary flux (F_λ) units. The dip at 2800 Å results from the lagged and smeared variability of the Mg II emission line with respect to the continuum and is widened by the errors in estimating the rest wavelength from the SDSS bands.

(A color version of this figure is available in the online journal.)

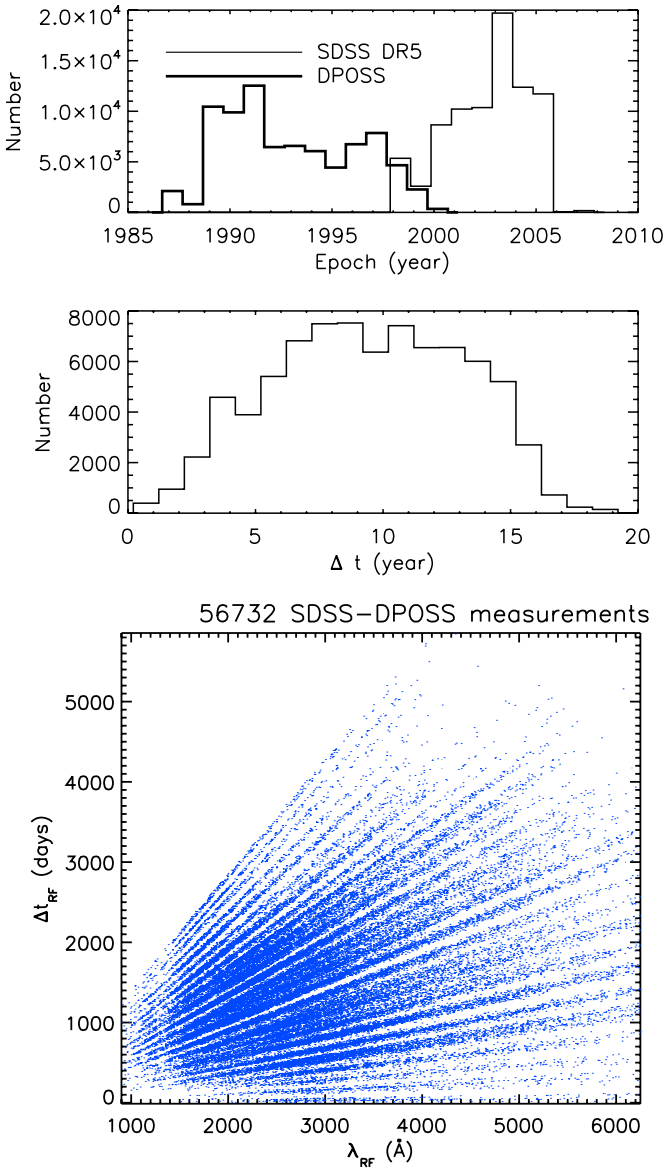

Figure 15. Top: distribution of epochs for the SDSS and DPOSS observations. Middle: distribution of the SDSS–DPOSS time lags in the observer's frame. Bottom: distribution of the SDSS–DPOSS time lags and wavelengths in the rest frame.

(A color version of this figure is available in the online journal.)

1. A bias in the measured τ (and thus SF_∞) values for S82 quasars due to insufficient light curve lengths. Since $\mathrm{SF}(\Delta t << \tau) = \hat{\sigma}\sqrt{|\Delta t|}$, $\hat{\sigma} = \mathrm{SF}_\infty/\sqrt{\tau}$ is the most strongly constrained quantity on timescales shorter than τ. That is, on a grid of $\log(\tau)$ versus $\log(\mathrm{SF}_\infty)$, the best-fit values will be scattered due to fitting errors along lines of constant $\hat{\sigma}$, but much less perpendicular to it (i.e., along lines of constant $K = \tau\sqrt{\mathrm{SF}_\infty}$). Therefore, as the light curve length decreases, the mean best-fit $\hat{\sigma}$ will not vary significantly, while the best-fit parameters τ, SF_∞, and K will become biased (see Kozł10; Mac10; MacLeod et al. 2011).
2. A bias in the deterministic model (Equation (6)). Due to the finite length of the S82 survey, 22% of the S82 sample was excluded from the analysis in Mac10 due to indeterminately long timescales. In this case, the measured parameters τ and SF_∞ are accurate for the remaining 78% of the S82 sample, but Equation (6) is only accurate for the lower values of τ ($\tau \lesssim 10^3$) and SF_∞ from which the correlations are derived.

In principle, both effects will lead to lower overall τ and SF_∞ in the distributions for S82 quasars, which will in turn cause the model ensemble SF to flatten at $\Delta t_{\mathrm{RF}} < 700$ days as seen here. Indeed, the excluded 22% of the sample will mostly contribute power to the long term rather than the short-term SF given their indeterminately long timescales. However, when simply including an additional population of long-τ objects to fill in the missing 22%, we are unable to quantitatively reproduce the last SDSS data point at $\Delta t_{\mathrm{RF}} = 1000$ days unless all the additional objects have $\tau \gtrsim 10{,}000$ days in the rest frame (while keeping the same distribution of $\hat{\sigma}$ as observed). On the other hand, if we double all the τ values in our model (instead of adding an extra population of quasars at long τ), while keeping $\hat{\sigma}$ fixed so that the SF_∞ values are multiplied by $\sqrt{2}$, we are able to reproduce the observed long-term SF, as shown by the agreement between the green lines in Figures 17 and 11 to the data points at long Δt_{RF}. In summary, the best-fit A coefficients from Equation (6) need to be altered upwards by 0.15 dex in the case of SF_∞, and by 0.30 dex in the case of τ, in order to explain the long timescale constraints provided by the SDSS–POSS data set.

At least half of these corrections can be understood as due to a fitting bias toward shorter τ (see Figure 7 in Mac10 and

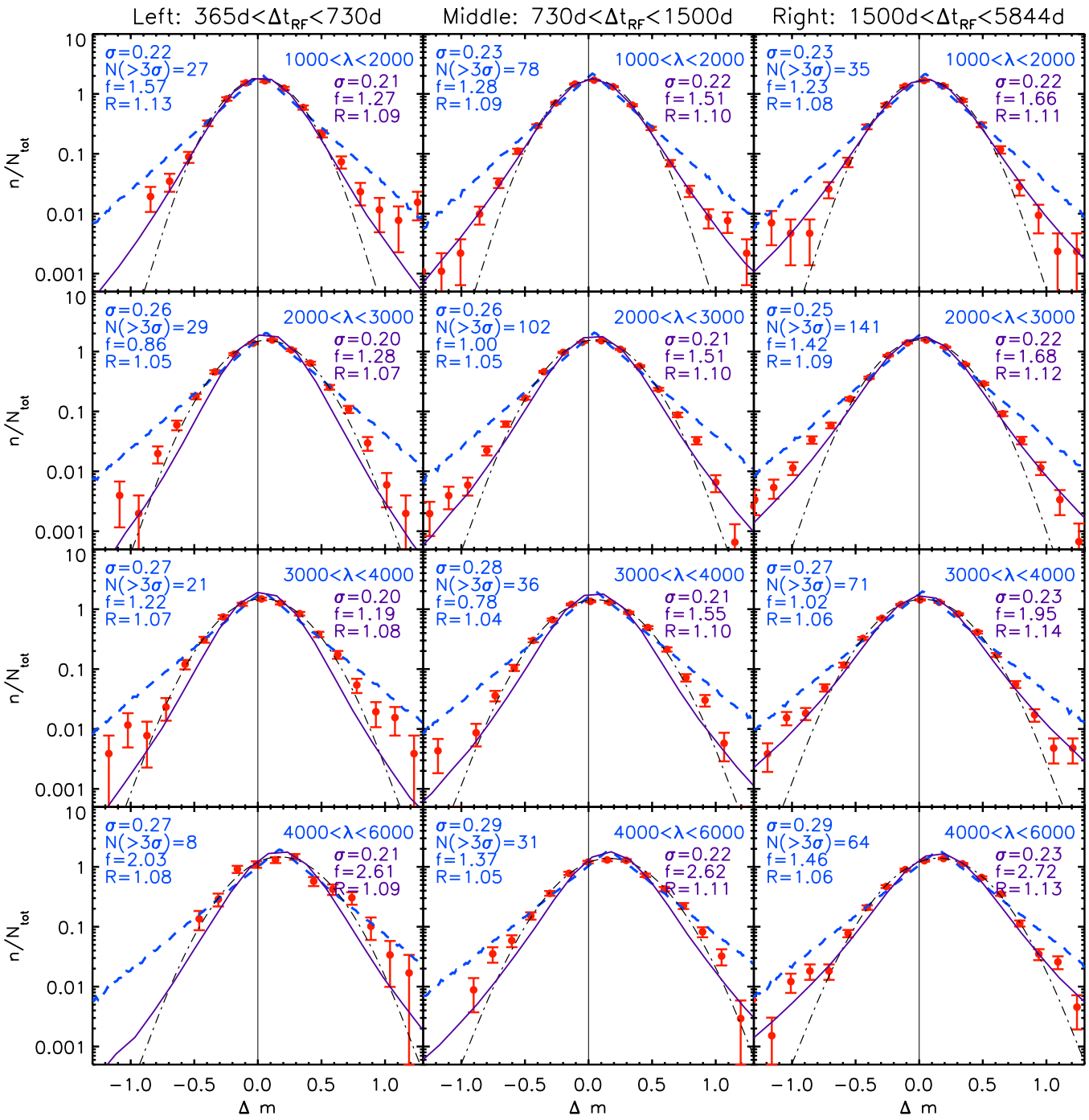

Figure 16. Similar to Figure 10 but for SDSS–DPOSS observations over the northern DR5 footprint (with $i < 19.1$ in SDSS). The photometric accuracy was assumed to be $\sigma_{\rm phot} = 0.1$ mag when computing the models. The Malmquist-like bias seen in the bottom panels is taken into account by shifting the model Δm distribution to the right by the observed mean.

(A color version of this figure is available in the online journal.)

Figure 15 in MacLeod et al. 2011). Another effect could be due to uncertain behavior for long timescales. The DRW process corresponds to a power spectral distribution (PSD) proportional to $1/f^2$ at frequencies $f > (2\pi\tau)^{-1}$, flattening to a constant at lower frequencies. Using the S82 data and computational technique described in Mac10, we were able to rule out an extrapolation of the $1/f^2$ power law. However, we were unable to distinguish between a $1/f^0$ or a $1/f$ PSD at frequencies $f < (2\pi\tau)^{-1}$, where the latter dependence is observed in X-ray PSDs for Galactic black holes as well as AGNs (McHardy et al. 2006; Kelly et al. 2011).

We compare the observed SF slopes from Voevodkin (2011), VB04, and Wilhite et al. (2008) to our data in the bottom panel of Figure 17. Voevodkin (2011) found that a broken power law provides a good fit to the S82 g-band ensemble SF with a slope of 0.33, steepening to 0.79 below 42 days. We also show the best-fit broken power law to our data with the break fixed to 42 days, and we find power-law indices at short and long Δt of 0.53 and 0.40, respectively. While our two-epoch SDSS data are consistent with the shallower slope of 0.33, our results do not support the conclusion of a much steeper SF(Δt) for small Δt found by Voevodkin (2011) for either the S82 or two-epoch data sets. We

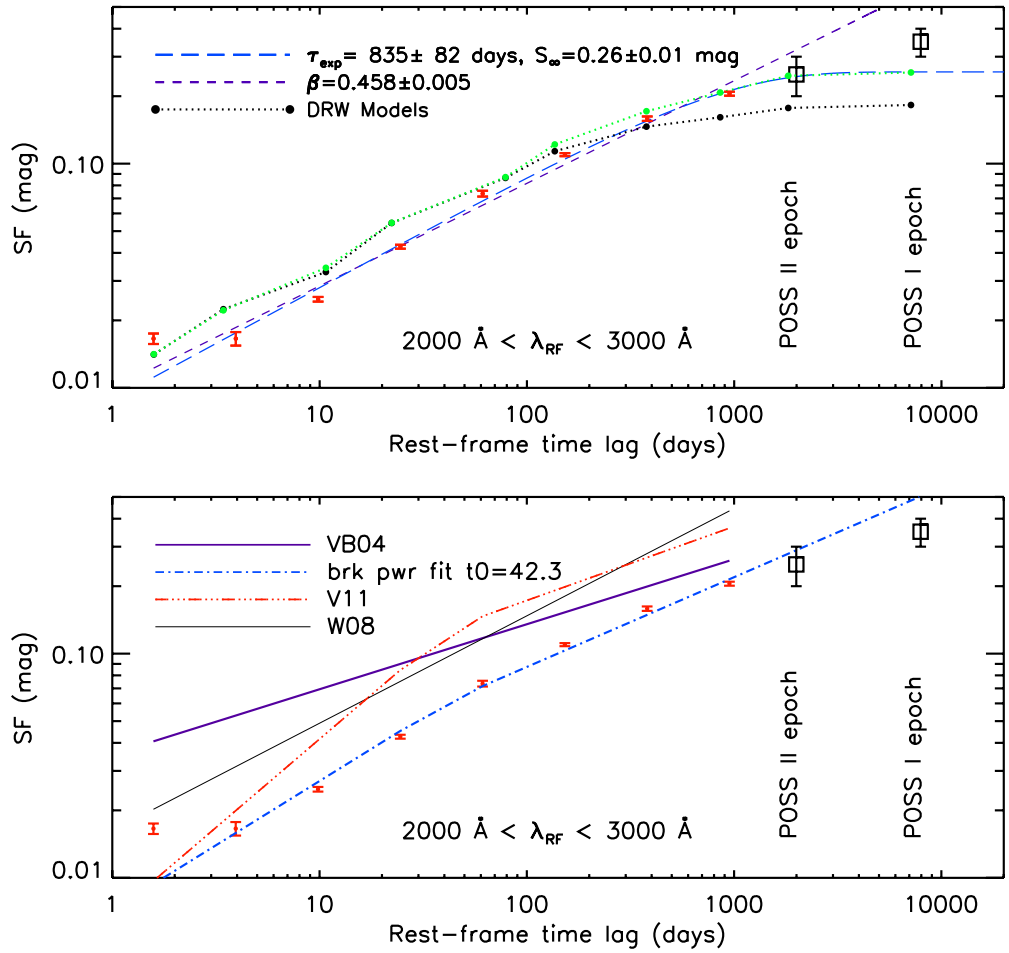

Figure 17. Top: similar to Figure 5, but plotted against the rest-frame time lag, for data with rest-frame wavelength in the range 2000–3000 Å. The data have been corrected for photometric errors by subtracting $0.018\sqrt{2}$ in quadrature. The green dotted line shows the prediction of the DRW model trained on S82 data with all τ and SF_∞ values multiplied by 2 and $\sqrt{2}$, respectively. Bottom: the data are shown along with comparison g-band fits from VB04 (purple line), Wilhite et al. (2008; thin line), and Voevodkin (2011; red dash-triple-dotted line). The normalization for these curves is arbitrary, since we are simply comparing the slopes. The blue dash-dotted line shows the best-fit broken power law to our data with the break set to 42.3 days, as in Voevodkin (2011).

(A color version of this figure is available in the online journal.)

interpret the broken power-law form to be a consequence of the turnover in the SF due to the mean characteristic timescale, as the observed SF is fully consistent with the form expected for a DRW (Equation (5)).

5. PREDICTIONS FOR FUTURE SURVEYS

Using the observed Δm distributions, we can predict the number of quasars with Δm exceeding an arbitrary limit that might be seen in a survey with a given number of quasars. This information is useful for transient identification, in particular to identify quasars that contaminate candidate lists of other objects. For example, Vanden Berk et al. (2002) reported an orphan gamma-ray burst afterglow based on a 2.5 mag decrease in the optical flux of an unidentified point source. Instead, as pointed out by Gal-Yam et al. (2002), the observations are best explained by the presence of a spectroscopically identified, highly variable quasar.

In order to quantify the importance of quasar contamination in future transient surveys, such as the PTF (Law et al. 2009) and the LSST (Ivezić et al. 2008), we need to know the probability that a quasar's brightness can increase by Δm (over the faint survey limit) within a time Δt. For example, assume that no source is detected above a faint limit of $m_{\rm faint}$ on a given night, but when repeating the observation some time later, a source is detected with magnitude $m = m_{\rm faint} - \Delta m$. In this case, we would like to know how many quasars with a Δm at least as large as that observed could be present in a particular scanned area and to a faint limit of $m_{\rm faint}$. Given that our stochastic model performs well at reproducing the observed ensemble variability of quasars, we can make robust and useful predictions for future surveys.

We make use of a mock LSST quasar sample which includes absolute B magnitudes (M_B) and redshifts generated over 100 deg^2 of sky using the luminosity function from Bongiorno et al. (2007) for the purposes of LSST image simulations. We limit the sample to $M_B < -20$ following Table 10.2 in the LSST Science Book (LSST Science Collaborations and LSST Project 2009). The distance modulus is computed assuming a standard cosmology: $\Omega_m = 0.27$, $\Omega_\Lambda = 0.73$, and $h = 0.71$. The LSST magnitudes (m) and rest-frame M_i (based on M_B) are computed using the composite quasar spectrum from Vanden Berk et al. (2001). The black hole masses are estimated from the M_i values using the prescription in Mac10.

We generate magnitude differences for each quasar in the mock LSST sample based on the DRW model most appropriate for the quasar's physical parameters, as described in Section 3.2.1. When computing the DRW model, the τ (SF_∞)

Table 1
Predicted Δm Probabilities for $m < 24.5$

Δt (days)	Band	$P(\Delta m > 1$ mag)	$P(\Delta m > 2$ mag)
3	u	$<2 \times 10^{-6}$	$<2 \times 10^{-6}$
3	r	$<2 \times 10^{-6}$	$<2 \times 10^{-6}$
3	z	$<2 \times 10^{-6}$	$<2 \times 10^{-6}$
30	u	7×10^{-5}	$<2 \times 10^{-6}$
30	r	4×10^{-6}	$<2 \times 10^{-6}$
30	z	$<2 \times 10^{-6}$	$<2 \times 10^{-6}$
300	u	0.02	6×10^{-4}
300	r	0.005	6×10^{-5}
300	z	0.002	1×10^{-5}

values are multiplied by 2 ($\sqrt{2}$) with respect to the expected values based on Mac10 in order to correct for the bias due to limited time sampling in S82 (see the previous section). We note that correcting for this bias should also account for at least some of the residual scatter in K estimated in Section 3.2.1; however, for simplicity we still include this scatter along with the bias correction in our simulations. First, we consider three different survey faint limits of $m_{\rm faint} = 19.1$ (to establish similarity with the SDSS results), $m_{\rm faint} = 22$, and $m_{\rm faint} = 24.5$, excluding all mock quasars with $m \geqslant m_{\rm faint}$ in each case. For the $m < 19.1$, 22, and 24.5 simulations, respectively, 1000, 100 and 11 model Δm values are generated per quasar to increase the sample size. A Gaussian noise component of width $\sqrt{2}\sigma_{\rm phot}$ is added to all curves to simulate a photometric accuracy similar to the SDSS (the photometric accuracy for future surveys such as LSST will likely be better than that for the SDSS, but this is a higher order question than investigated here). Note that we retain all Δm values in the simulations, including $|\Delta m| > 3$.

Figure 18 shows the simulated cumulative distribution of Δm in the urz bands for three faint magnitude limits. Also shown are Gaussian analytic functions as thin curves with the same rms as the data. Using these cumulative distributions, which are based on $\sim 10^6$ mock quasars, we predict probabilities down to our resolution limit ($P \gtrsim 10^{-6}$). Table 1 lists the predicted probabilities of observing a quasar with $m < 24.5$ and a magnitude difference of $\Delta m > 1$ mag and $\Delta m > 2$ mag over 3, 30, and 300 days, using the observed frame, in the urz bands. Due to the exponential nature of the Δm distributions, the probability of observing $\Delta m > 1$ mag reaches 0.02 in the u band (where variability is strongest) for time lags of 300 days, and 6×10^{-4} for $\Delta m > 2$ mag. Assuming Gaussian Δm distributions will result in erroneous probability estimates of 9×10^{-4} and 10^{-6}, respectively.

Next, we adopt realistic PTF photometric errors which vary as a function of magnitude, and repeat the simulation in g and r using the PTF magnitude limits ($r < 20.6$ and $g < 21.0$). The errors range from 0.008 mag at the brightest limits to 0.2 mag at the faint end. As shown in Figure 19, the resulting distributions are more Gaussian than those in the previous simulations due to the different dependence of errors on magnitude. However, at extreme values of Δm, the Gaussian curves significantly underestimate the detection probabilities in both g and r.

These results would have been useful to Vanden Berk et al. (2002), who reported a single transient with $\Delta m = 2.5$ mag over 410 days in the gri bands in early SDSS data covering 1500 deg^2. Since the object had the spectrum of a normal galaxy in its faint phase (rather than a nonstellar spectrum with broad emission lines indicative of quasars), the authors concluded that

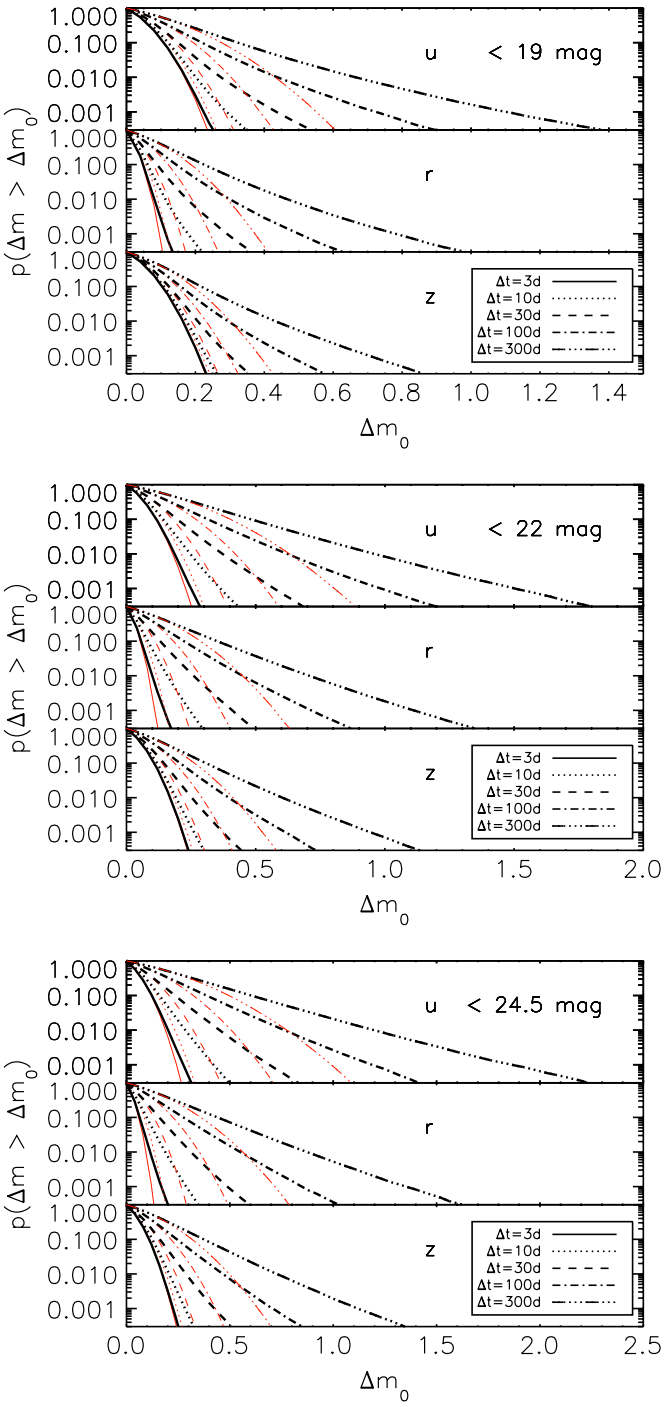

Figure 18. Predicted cumulative distribution of magnitude differences in u, r, and z bands as a function of observed time lag (Δt) for $\sim$1 million quasars with magnitudes less than 19.1 (top three panels), 22 (middle three panels), and 24.5 (bottom three panels). The thin curves show the Gaussian distributions with the same rms widths.

(A color version of this figure is available in the online journal.)

it was more likely to be a gamma-ray burst afterglow than a highly variable quasar, given the large drop in flux. We find that the probability of a quasar having $\Delta m = 2.5$ mag over 410 days with $m_{\rm faint} = 22$ is 10^{-5} in the g and r bands. To find the number of quasars expected to exhibit this variability in 1500 deg^2 of sky, one needs to know the quasar density. We extrapolate Figure 13 in Richards et al. (2006) to a density of $\sim$120 deg^{-2} at $i < 22$. Therefore, we expect roughly

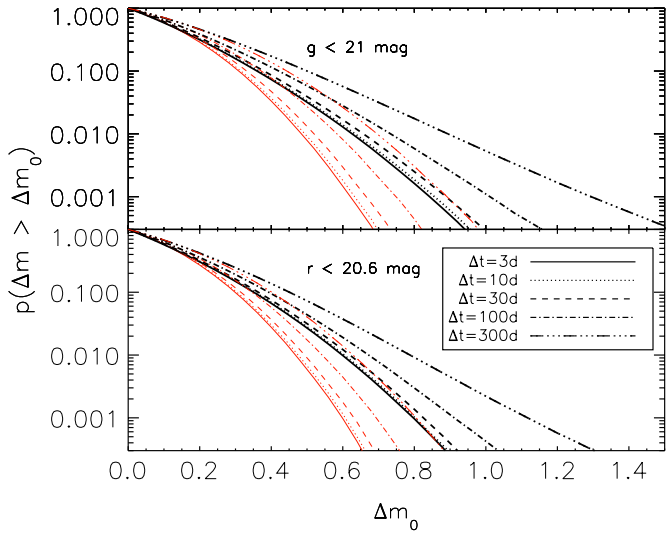

Figure 19. Predicted cumulative distribution of *g*-band (top) and *r*-band (bottom) magnitude differences, including realistic PTF photometric errors as a function of observed time lag (Δt) for quasars brighter than the PTF magnitude limit ($g < 21.0$ and $r < 20.6$). The thin curves show the Gaussian distributions with the same rms widths.

(A color version of this figure is available in the online journal.)

10^5 quasars in 1500 deg^2 to $i < 22$. Given a probability of 10^{-5}, we expect that roughly one quasar will show $\Delta r = 2.5$ mag over $\Delta t = 410$ days in the SDSS sample studied by Vanden Berk et al. (2002). This is consistent with their finding, and with the follow-up study of Gal-Yam et al. (2002) who confirmed that it is indeed a highly variable quasar. If one assumes a Gaussian distribution of Δm, the probability is less than 10^{-6}, and one would expect $\lesssim$0.1 quasar to be found with these parameters. Given this expectation value, the probability to detect one quasar is at most 0.09, and the quasar hypothesis can be (erroneously) rejected at a $\gtrsim 2\sigma$ level.

6. DISCUSSION

We have assembled, organized, and publicly released a data set including ~3.5 million photometric measurements for 80,000 spectroscopically confirmed quasars. The available time lags span 0.8 days to almost 20 years in the observer's frame. We have analyzed and quantified the observed variability in the observer's and rest frames. By assuming a DRW model for each quasar in our sample, we reconcile the observed variability of individual quasars in S82 with their ensemble statistics. Our principal results are as follows.

1. Long-term quasar variability measurements, constrained using SDSS and POSS data for time lags of up to 50 years (in the observer's frame), conclusively show that a simple power-law dependence for the SF cannot be extrapolated beyond a decade, and suggests an average characteristic timescale for quasar variability in the rest frame of ~2 years and an average long-term dispersion of ~0.26 mag (for rest wavelengths 2000–3000 Å). This behavior extrapolates well to the UV results of Welsh et al. (2011), who find that the SF for *GALEX* NUV data reaches about 0.4 mag and flattens at $\Delta t_{\rm RF} > 300$ days. This SF limit corresponds to a limiting SF value of 0.33 mag when using our definition of the SF (see Section 3.1.2), and 0.27 mag when also scaling to the *u* band using the wavelength dependence from Equation (6). This result is in close agreement with the SF at the shortest wavelengths in our data set. Voevodkin (2011) found that a broken power law provides a good fit to the S82 ensemble SF with a slope of 0.33 at long timescales steepening to 0.79 below 42 days. Our two-epoch SDSS data are consistent with the shallower slope of 0.33, but our data do not support the conclusion of a much steeper SF(Δt) for small Δt found by Voevodkin (2011). While we cannot rule out a broken power-law dependence with the available data, the observed SF is fully consistent with the form expected for a DRW (Equation (5)).
2. We tested the DRW model results based on SDSS S82 data on an independent data set, and confirm that the variability parameters τ and SF$_\infty$ correlate with physical parameters as found for individual quasars (e.g., Mac10, and references therein). This is evident from the agreement of our model with the observed ensemble variability of SDSS quasars. However, the results indicate that the measured τ and SF$_\infty$ distributions are biased low for the S82 sample by a factor of about 2 and $\sqrt{2}$, respectively. This bias most likely results from the 10 year length limit of the S82 light curves, although it could also be due to uncertain behavior for long timescales. The best-fit *A* coefficients from Equation (6) (Mac10) need to be shifted upward by 0.15 dex in the case of SF$_\infty$, and by 0.30 dex in the case of τ, in order to explain the long timescale constraints provided by the SDSS–POSS data set. These shifts leave the shorter timescale variability statistics unchanged.
3. For a given time lag and wavelength, the magnitude difference (Δm) distribution is exponential rather than Gaussian for large magnitude changes. This is well explained as a cumulative effect of averaging over quasars with a range of different τ and SF$_\infty$. This is a remarkable result given that the Δm distribution of every individual quasar is Gaussian.
4. We made predictions for the incidence of quasar contamination in transient surveys using detailed simulations of quasar light curves from a mock LSST catalog. Due to the exponential nature of the Δm distributions for quasars, the probability of observing $\Delta m > 1$ mag reaches 0.02 in the *u* band (where variability is strongest) for time lags of 300 days, and 6×10^{-4} for $\Delta m > 2$ mag. Assuming Gaussian Δm distributions will result in erroneous likelihood estimates that are about 10 and 1000 times smaller, respectively.

It is clear that a major limitation for the S82 quasars is the quality of light curves in both sampling density and time span. It is also clear that our variability model needs to be better tested given the evidence for a likely bias in the S82 timescale estimates. The best current sample for these improvements is that from the OGLE microlensing survey, since the light curves are more densely sampled and longer than for S82. Here, the problem is the lack of spectroscopic identification of quasar candidates, although the follow-up confirmation of quasars is rapidly improving (Kozłowski et al. 2012). The next-generation surveys will also greatly improve the constraints on the long-term SF both individually and for ensembles of quasars. The best short-term prospects are PTF (Law et al. 2009), Pan-STARRS (Kaiser et al. 2002), and the Dark Energy Survey (DES; Honscheid et al. 2008). In particular, the DES supernova program will greatly expand many of the S82 quasar light curves with *griz* sampling once per week for ~3 months per year over 5 years. The combination of SDSS, Pan-STARRS, DES, and LSST will yield well-sampled light curves covering over 25 years for 10,000 quasars in S82.

Table 2
Northern Survey: Catalog Format

Column	Format	Units	Description
1	I6	···	Row of DR7 Quasar Catalog V (out of 105783)
2	F7.3	mag	Absolute i-band magnitude[a]
3	F6.4	···	Redshift
4	F6.3	$M_\odot$	Black hole mass ("0" means none could be found)[b]
5	F6.3	erg s^{-1}	Bolometric luminosity[b]
6	F6.3	mag	Galactic extinction in u filter (from Schlegel et al. 1998)[c]
7	F7.3	mag	FIRST peak 20 cm flux density[d]
8	F8.3	···	Signal-to-noise ratio for FIRST flux density
9	F8.3	ct s^{-1}	RASS BSC/FSC full band count rate[e]
10	F7.3	···	Signal-to-noise ratio for RASS count rate
11	F7.3	mag	2MASS J-band magnitude[f]
12	F6.3	mag	Error in J
13	F7.3	mag	2MASS H-band magnitude[f]
14	F6.3	mag	Error in H
15	F7.3	mag	2MASS K-band magnitude[f]
16	F6.3	mag	Error in K
17	I3	···	Total number of observations
18	I1	···	Flag for Stripe 82 object[g]
19	F9.3	days	Modified Julian Date of imaging observation
20	F6.3	mag	BEST SDSS u-band PSF magnitude[h]
21	F6.3	mag	Error in u
22	F6.3	mag	BEST SDSS g-band PSF magnitude[h]
23	F6.3	mag	Error in g
24	F6.3	mag	BEST SDSS r-band PSF magnitude[h]
25	F6.3	mag	Error in r
26	F6.3	mag	BEST SDSS i-band PSF magnitude[h]
27	F6.3	mag	Error in i
28	F6.3	mag	BEST SDSS z-band PSF magnitude[h]
29	F6.3	mag	Error in z
···	···	···	Fields 19–29 repeated for each additional observation

Notes.
[a] For $\Omega_m = 0.300$, $\Omega_\Lambda = 0.700$, $h = 0.70$, and $\alpha_Q = -0.50$.
[b] Taken from the Shen et al. (2011) catalog.
[c] Where $A_g, A_r, A_i, A_z = 0.736, 0.534, 0.405, 0.287 \times A_u$, respectively.
[d] In AB magnitudes; $-2.5 \log(f_\nu/3631\,\mathrm{Jy})$.
[e] X-ray data from ROSAT All Sky Survey Bright and Faint source catalogs. A value of -9.000 indicates a non-detection.
[f] All 2MASS data are from the 2MASS All-Sky Data Release Point Source Catalog (PSC) as of 2003 March 25. Note that 2MASS measurements are Vega-based, not AB, magnitudes. A value of 0.000 indicates a non-detection.
[g] A value of 1 (0) indicates a (non-)Stripe 82 source.
[h] SDSS photometric measurements are asinh magnitudes (Lupton et al. 1999) and are normalized (to ∼3% accuracy) to the AB-magnitude system (Oke & Gunn 1983). Uncorrected for Galactic extinction. A value of 0.000 indicates that the value could not be retrieved from the SDSS database.

The success of the model presented here suggests that a range of characteristic timescales exists among an ensemble of quasars, which can be related to physical timescales in the accretion disk. While we assumed a single τ per quasar, there is evidence that multiple timescales can exist for a given quasar (Collier & Peterson 2001; Kelly et al. 2011). Therefore, the study presented here can be extended to adopt the model in Kelly et al. (2011), which fits more than one τ for a given object. This model, also called a mixed Ornstein–Uhlenbeck (OU) process, reproduces a PSD of the form exhibited by the X-ray light curves of galactic black holes and AGNs, which is flat below a low-frequency break, decays as $1/f$ above the low-frequency break, and steepens to $1/f^2$ above a high-frequency break. In this case, with two characteristic timescales for each quasar, the long-term ensemble SF can be revisited and possibly explained in the context of a mixed OU process. Note that recent optical data from the *Kepler* mission (Mushotzky et al. 2011), which have a sampling of 1 data point roughly every 30 minutes and 0.1% errors, suggest an additional break to a steeper slope ($\sim 1/f^3$), but this dependence is seen on timescales shorter than can be resolved in SDSS data.

We acknowledge support by NSF Grant AST-0807500 to the University of Washington, and NSF Grant AST-0551161 to LSST for design and development activity. B.S. would like to acknowledge NSF grant AST-0908139 awarding to Judy Cohen for partial support. C.S.K. is supported by NSF Grant AST-1009756. We thank the referee for a thorough review and suggestions which led to an improved manuscript.

Funding for the SDSS and SDSS-II has been provided by the Alfred P. Sloan Foundation, the Participating Institutions, the National Science Foundation, the U.S. Department of Energy, the National Aeronautics and Space Administration, the Japanese Monbukagakusho, the Max Planck Society, and the Higher Education Funding Council for England. The SDSS Web Site is http://www.sdss.org/.

The SDSS is managed by the Astrophysical Research Consortium for the Participating Institutions. The Participating

Table 3
Southern Survey: Catalog Format

Column	Format	Units	Description
1	I7	···	The name of the light curve file
2	F10.6	deg	Median right ascension in decimal degrees (J2000)
3	F10.6	deg	Median declination in decimal degrees (J2000)
4	I5	···	Row of DR5 Quasar Catalog IV (out of 77429)
5	F7.3	mag	Absolute i-band magnitude, K-corrected to $z = 0$[a]
6	F7.3	mag	Absolute i-band magnitude, K-corrected to $z = 2$[b]
7	F6.4	···	Redshift
8	F5.3	$M_\odot$	Black hole mass ("0.000" means none could be found)[b]
9	F6.3	erg s^{-1}	Bolometric luminosity[b]
10	F6.3	mag	SDSS BEST u-band PSF magnitude[c]
11	F6.3	mag	SDSS BEST g-band PSF magnitude[c]
12	F6.3	mag	SDSS BEST r-band PSF magnitude[c]
13	F6.3	mag	SDSS BEST i-band PSF magnitude[c]
14	F6.3	mag	SDSS BEST z-band PSF magnitude[c]
15	F6.3	mag	Galactic extinction in u filter (from Schlegel et al. 1998)[d]

Notes.
[a] For $\Omega_m = 0.300$, $\Omega_\Lambda = 0.700$, $h = 0.70$, and $\alpha_Q = -0.50$.
[b] Taken from the Shen et al. (2008) catalog. A value of "−1" indicates a newly confirmed DR7 quasar, and thus is not present in Shen et al. (2008) (see the latest version, Shen et al. 2011, for the values).
[c] SDSS photometric measurements are asinh magnitudes (Lupton et al. 1999) and are normalized (to ∼3% accuracy) to the AB-magnitude system (Oke & Gunn 1983). Uncorrected for Galactic extinction. A value of 0.000 indicates that the value could not be retrieved from the SDSS database.
[d] Where $A_g, A_r, A_i, A_z = 0.736, 0.534, 0.405, 0.287 \times A_u$, respectively. This value is set to zero if it is a newly confirmed DR7 quasar (see the DR7 Quasar Catalog V for the true values).

Table 4
Southern Survey: Light Curve File Format

Column	Format	Units	Description
1	D	days	Modified Julian Date for u-band observation
2	F6.3	mag	Apparent u-band magnitude[a]
3	F5.3	mag	Error in u
4	D	days	Modified Julian Date for g-band observation
5	F6.3	mag	Apparent g-band magnitude[a]
6	F5.3	mag	Error in g
7	D	days	Modified Julian Date for r-band observation
8	F6.3	mag	Apparent r-band magnitude[a]
9	F5.3	mag	Error in r
10	D	days	Modified Julian Date for i-band observation
11	F6.3	mag	Apparent i-band magnitude[a]
12	F5.3	mag	Error in i
13	D	days	Modified Julian Date for z-band observation
14	F6.3	mag	Apparent z-band magnitude[a]
15	F5.3	mag	Error in z
16	D	deg	Median right ascension in decimal degrees (J2000)[b]
17	D	deg	Median declination in decimal degrees (J2000)

Notes.
[a] Not corrected for Galactic absorption. Bad observations are printed as "−99.99."
[b] 360 deg is subtracted from all R.A. values exceeding 300 deg.

Institutions are the American Museum of Natural History, Astrophysical Institute Potsdam, University of Basel, University of Cambridge, Case Western Reserve University, University of Chicago, Drexel University, Fermilab, the Institute for Advanced Study, the Japan Participation Group, Johns Hopkins University, the Joint Institute for Nuclear Astrophysics, the Kavli Institute for Particle Astrophysics and Cosmology, the Korean Scientist Group, the Chinese Academy of Sciences (LAMOST), Los Alamos National Laboratory, the Max-Planck-Institute for Astronomy (MPIA), the Max-Planck-Institute for Astrophysics (MPA), New Mexico State University, Ohio State University, University of Pittsburgh, University of Portsmouth, Princeton University, the United States Naval Observatory, and the University of Washington.

APPENDIX

THE CATALOG FORMAT

Here, we present a database of ∼3.5 million photometric measurements for 80,000 spectroscopically confirmed quasars to be used for time variability studies. The database consists of three different data sets: two with repeated SDSS imaging in

Table 5
SDSS–DPOSS: Catalog Format

Column	Format	Units	Description
1	F10.6	deg	Right ascension in decimal degrees (J2000)
2	F10.6	deg	Declination in decimal degrees (J2000)
3	I3	···	DPOSS Plate ID
4	F9.4	yr	Epoch of the DPOSS observation in the *G* band
5	F9.4	yr	Epoch of the DPOSS observation in the *R* band
6	F9.4	yr	Epoch of the DPOSS observation in the *I* band
7	F6.2	mag	DPOSS catalog *G* magnitude[a]
8	F6.2	mag	Error in *G*
9	F6.2	mag	*G*-band quality flag[b]
10	F6.2	mag	DPOSS catalog *R* magnitude[a]
11	F6.2	mag	Error in *R*
12	F6.2	mag	*R*-band quality flag[b]
13	F6.2	mag	DPOSS catalog *I* magnitude[a]
14	F6.2	mag	Error in *I*
15	I1	mag	*I*-band quality flag[b]
16	I6	···	Row of DR7 Quasar Catalog V (out of 105783)
17	F7.3	mag	Absolute *i*-band magnitude[c]
18	F6.4	···	Redshift
19	F6.3	$M_\odot$	Black hole mass ("0.000" means none could be found)[d]
20	F6.3	erg s^{-1}	Bolometric luminosity[d]
21	F6.3	mag	Galactic extinction in *u* filter (from Schlegel et al. 1998)[e]
22	I1	···	Number of observations
23	I1	···	Flag for Stripe 82 object[f]
24	I5	days	Modified Julian Date for SDSS imaging observation
25	F6.3	mag	BEST SDSS *g*-band PSF magnitude[g]
26	F6.3	mag	Error in *g*
27	F6.3	mag	BEST SDSS *r*-band PSF magnitude[g]
28	F6.3	mag	Error in *r*
29	F6.3	mag	BEST SDSS *i*-band PSF magnitude[g]
30	F6.3	mag	Error in *i*

Notes.
[a] Not corrected for Galactic absorption. Bad observations are printed as "−99.99."
[b] Flag indicating whether the recalibrated magnitude is of good quality (a value of 1 is "good"). See Ses06 for a description of these cuts.
[c] For $\Omega_m = 0.300$, $\Omega_\Lambda = 0.700$, $h = 0.70$, and $\alpha_Q = -0.50$.
[d] Taken from the Shen et al. (2011) catalog.
[e] Where $A_g, A_r, A_i, A_z = 0.736, 0.534, 0.405, 0.287 \times A_u$, respectively.
[f] A value of 1 (0) indicates a (non-)Stripe 82 source.
[g] SDSS photometric measurements are asinh magnitudes (Lupton et al. 1999) and are normalized (to ∼3% accuracy) to the AB-magnitude system (Oke & Gunn 1983). Uncorrected for Galactic extinction. A value of 0.000 indicates that the value could not be retrieved from the SDSS database.

five UV-to-IR photometric bands, and one with SDSS versus POSS imaging for three bands. The observed time lags span the range from 0.8 days to 10 years for the SDSS data sets, and up to 20 years for the SDSS versus DPOSS data set. The three data sets are described below.

1. *Northern Survey.* The SDSS imaging data are obtained by drift scanning. Because of the scan overlaps, and because of the scan convergence near the survey poles, about 40% of the northern survey area (∼4000 deg^2) is surveyed at least twice. This method provides two-epoch five-band coverage for ∼25,000 spectroscopically confirmed quasars. We adopt the SDSS BEST photometry listed in the DR7 Quasar Catalog V (Schneider et al. 2010) for the primary observations, and we searched for all unresolved secondary observations within 1 arcsec of the primary using CasJobs. Here, we include all observations up to three per quasar (only 0.2% of the sample had more than three observations). We also include the redshifts, absolute magnitudes, FIRST, RASS, and 2MASS photometry as listed in the DR7 Quasar Catalog V, and the black hole masses as measured from emission line widths by Shen et al. (2011). The catalog format is found in Table 2. We also provide a list of all the objects (in the same order) with the same exact format as the DR7 Quasar Catalog V (Table 2 in Schneider et al. 2010).
2. *Southern Survey.* About 290 deg^2 of the southern survey area has already been observed ∼60 times to search for variable objects and, by stacking the frames, to go deeper. This is the SDSS S82, which is $22^h24^m <$ R.A. $< 04^h08^m$ and |decl.| < 1.27 deg. These multi-epoch data have timescales ranging from 3 hr to almost 10 years. This method provides well-sampled five-band light curves for an unprecedented number of quasars (9258). The catalog format is found in Table 3, and the light curve file format is found in Table 4. We also provide a list of all the objects (in the same order) with the same exact format as the DR5 Quasar Catalog IV (Table 2 in Schneider et al. 2007).
3. *SDSS–DPOSS.* We also include a catalog of all SDSS DR7 quasars with DPOSS observations. Following the procedure outlined in Sesar et al. (2006), we have recalibrated DPOSS

data (Djorgovski et al. 1998) in 8000 deg^2 of sky from the SDSS Data Release 5. The main advantage of this data set, which includes 81,189 quasars, is its long time baseline of 20 years. Here, we present the SDSS–DPOSS photometry in GRI bands, where the latter is accurate to 0.10–0.15 mag. The catalog format is presented in Table 5.

For more details, see http://www.astro.washington.edu/users/ivezic/macleod/qso_dr7/.

REFERENCES

Abazajian, K. N., Adelman-McCarthy, J. K., Ageros, M. A., et al. 2009, ApJS, 182, 543
Ai, Y. L., Yuan, W., Zhou, H. Y., et al. 2010, ApJ, 716, L31
Annis, J., Soares-Santos, M., Strauss, M. A., et al. 2011, arXiv:1111.6619
Bauer, A., Baltay, C., Coppi, P., et al. 2009, ApJ, 696, 1241
Bauer, A. H., Seitz, S., Jerke, J., et al. 2011, ApJ, 732, 64
Bongiorno, A., Zamorani, G., Gavignaud, I., et al. 2007, A&A, 472, 443
Butler, N. R., & Bloom, J. S. 2011, AJ, 141, 93
Collier, S., & Peterson, B. M. 2001, ApJ, 555, 775
de Vries, W. H., Becker, R. H., & White, R. L. 2003, AJ, 126, 1217
de Vries, W. H., Becker, R. H., White, R. L., & Loomis, C. 2005, AJ, 129, 615 [dV05]
Dexter, J., & Agol, E. 2011, ApJ, 727, L24
Djorgovski, S. G., Gal, R. R., Odewahn, S. C., et al. 1998, in 14th IAP Meeting, Wide Field Surveys in Cosmology, ed. S. Colombi, Y. Mellier, & B. Raban (Paris: Editions Frontieres), 89
Frieman, J. A., Bassett, B., Becker, A., et al. 2008, AJ, 135, 338
Fukugita, M., Ichikawa, T., Gunn, J. E., et al. 1996, AJ, 111, 1748
Gal-Yam, A., Ofek, E. O., Filippenko, A. V., Chornock, R., & Li, W. 2002, PASP, 114, 587
Giveon, U., Maoz, D., Kaspi, S., Netzer, H., & Smith, P. S. 1999, MNRAS, 306, 637
Gunn, J. E., Carr, M., Rockosi, C., et al. 1998, AJ, 116, 3040
Hawkins, M. R. S. 1983, MNRAS, 202, 571
Hawkins, M. R. S. 2002, MNRAS, 329, 76
Hawkins, M. R. S., & Veron, P. 1995, MNRAS, 275, 1102
Honscheid, K., DePoy, D. L., & for the DES Collaboration 2008, arXiv:0810.3600
Hook, I. M., McMahon, R. G., Boyle, B. J., & Irwin, M. J. 1994, MNRAS, 268, 305
Hughes, P. A., Aller, H. D., & Aller, M. F. 1992, ApJ, 396, 469
Ivezić, Z., Lupton, R., Johnston, D., et al. 2004a, in ASP Conf. Ser. 311, AGN Physics with the Sloan Digital Sky Survey, ed. G. T. Richards & P. B. Hall (San Francisco, CA: ASP), 437
Ivezić, Ž., Lupton, R. H., Anderson, S., et al. 2003, Mem. Soc. Astron. Ital., 74, 978
Ivezić, Ž., Lupton, R. H., Juric, M., et al. 2004b, in IAU Symp. 222, The Interplay Among Black Holes, Stars and ISM in Galactic Nuclei, ed. T. Storchi-Bergmann, L. C. Ho, & H. R. Schmitt (Cambridge: Cambridge Univ. Press), 525 [I04]
Ivezić, Ž., Lupton, R. H., Schlegel, D., et al. 2004c, Astron. Nachr., 325, 583
Ivezić, Z., et al. 2008, arXiv:0805.2366
Kaiser, N., Aussel, H., Burke, B. E., et al. 2002, Proc. SPIE, 4836, 154
Kawaguchi, T., Mineshige, S., Umemura, M., & Turner, E. L. 1998, ApJ, 504, 671
Kelly, B. C., Bechtold, J., & Siemiginowska, A. 2009, ApJ, 698, 895 [KBS09]
Kelly, B. C., Sobolewska, M., & Siemiginowska, A. 2011, ApJ, 730, 52
Kozłowski, S., & Kochanek, C. S. 2009, ApJ, 701, 508
Kozłowski, S., Kochanek, C. S., Jacyszyn, A. M., et al. 2012, ApJ, 746, 27
Kozłowski, S., Kochanek, C. S., Stern, D., et al. 2010a, ApJ, 716, 530
Kozłowski, S., Kochanek, C. S., Udalski, A., et al. 2010b, ApJ, 708, 927 [Kozł10]
Kozłowski, S., Kochanek, C. S., & Udalski, A. 2011, ApJS, 194, 22
Law, N. M., Kulkarni, S. R., Dekany, R. G., et al. 2009, PASP, 121, 1395
LSST Science Collaborations and LSST Project 2009, LSST Science Book, Version 2.0 (arXiv:0912.0201), http://www.lsst.org/lsst/scibook
Lupton, R. H., Gunn, J. E., Ivezić, Z., et al. 2001, in ASP Conf. Proc. 238, Astronomical Data Analysis Software and Systems X, ed. F. R. Harnden, Jr., F. A. Primini, & H. E. Payne (San Francisco, CA: ASP), 269
Lupton, R. H., Gunn, J. E., & Szalay, A. 1999, AJ, 118, 1406
Lyubarskii, Y. E. 1997, MNRAS, 292, 679
MacLeod, C. L., Brooks, K., Ivezić, Ž., et al. 2011, ApJ, 728, 26
MacLeod, C., Ivezić, Ž., de Vries, W., Sesar, B., & Becker, A. 2008, in AIP Conf. Ser. 1082, Classification and Discovery in Large Astronomical Surveys, ed. C. A. L. Bailer-Jones (Melville, NY: AIP), 282
MacLeod, C. L., Ivezić, Ž., Kochanek, C. S., et al. 2010, ApJ, 721, 1014 [Mac10]
Mahabal, A. A., Djorgovski, S. G., Graham, M. J., et al. 2005, in ASP Conf. Ser. 347, Astronomical Data Analysis Software and Systems XIV, ed. P. Shopbell, M. Britton, & R. Ebert (San Francisco, CA: ASP), 604
Matthews, T. A., & Sandage, A. R. 1963, ApJ, 138, 30
McHardy, I. M., Koerding, E., Knigge, C., Uttley, P., & Fender, R. P. 2006, Nature, 444, 730
Meusinger, H., Hinze, A., & de Hoon, A. 2011, A&A, 525, A37
Minkowski, R. L., & Abell, G. O. 1963, in Stars and Stellar Systems, Vol. 3, Basic Astronomical Data, ed. K. A. Strand (Chicago, IL: Univ. Chicago Press), 481
Morgan, C. W., Kochanek, C. S., Morgan, N. D., & Falco, E. E. 2010, ApJ, 712, 1129
Mushotzky, R. F., Edelson, R., Baumgartner, W. H., & Gandhi, P. 2011, ApJ, 743, L12
Oke, J. B., & Gunn, J. E. 1983, ApJ, 266, 713
Pier, J. R., Munn, J. A., Hindsley, R. B., et al. 2003, AJ, 125, 1559
Reichert, G. A., Rodriguez-Pascual, P. M., Alloin, D., et al. 1994, ApJ, 425, 582
Rengstorf, A. W., Brunner, R. J., & Wilhite, B. C. 2006, AJ, 131, 1923
Rengstorf, A. W., Mufson, S. L., Andrews, P., et al. 2004, ApJ, 617, 184
Richards, G. T., Fan, X., Newberg, H. J., et al. 2002, AJ, 123, 2945
Richards, G. T., Strauss, M. A., Fan, X., et al. 2006, AJ, 131, 2766
Schlegel, D., Finkbeiner, D. P., & Davis, M. 1998, ApJ, 500, 525
Schmidt, K. B., Rix, H.-W., Shields, J. C., et al. 2012, ApJ, 744, 147
Schneider, D. P., Hall, P. B., Richards, G. T., et al. 2007, AJ, 134, 102
Schneider, D. P., Richards, G. T., Hall, P. B., et al. 2010, AJ, 139, 2360
Sesar, B., Ivezić, Ž., Lupton, R. H., et al. 2007, AJ, 134, 2236
Sesar, B., Svilković, D., Ivezić, Ž., et al. 2006, AJ, 131, 2801 [Ses06]
Shen, Y., Greene, J. E., Strauss, M. A., Richards, G. T., & Schneider, D. P. 2008, ApJ, 680, 169
Shen, Y., Richards, G. T., Strauss, M. A., et al. 2011, ApJS, 194, 45
Smith, J. A., Tucker, D. L., Kent, S., et al. 2002, AJ, 123, 2121
Stoughton, C., Lupton, R. H., Bernardi, M., et al. 2002, AJ, 123, 485
Trevese, D., Kron, R. G., & Bunone, A. 2001, ApJ, 551, 103
Udalski, A., Kubiak, M., & Szymanski, M. 1997, Acta Astron., 47, 319
Udalski, A., Szymanski, M. K., Soszynski, I., & Poleski, R. 2008, Acta Astron., 58, 69
van den Bergh, S., Herbst, E., & Pritchet, C. 1973, AJ, 78, 375
Vanden Berk, D. E., Lee, B. C., Wilhite, B. C., et al. 2002, ApJ, 576, 673
Vanden Berk, D. E., Richards, G. T., Bauer, A., et al. 2001, AJ, 122, 549
Vanden Berk, D. E., Wilhite, B. C., Kron, R. G., et al. 2004, ApJ, 601, 692 [VB04]
Voevodkin, A. 2011, arXiv:1107.4244
Welsh, B. Y., Wheatley, J. M., & Neil, J. D. 2011, A&A, 527, A15
Wilhite, B. C., Brunner, R. J., Grier, C. J., Schneider, D. P., & vanden Berk, D. E. 2008, MNRAS, 383, 1232
Wilhite, B. C., Vanden Berk, D. E., Kron, R. G., et al. 2005, ApJ, 633, 638
York, D. G., Adelman, J., Anderson, J. E., Jr., et al. 2000, AJ, 120, 1579
Zu, Y., Kochanek, C. S., Kozłowski, S., & Udalski, A. 2012, arXiv:1202.3783